

# THE ROLE OF TURBULENCE IN SETTING THE PHASE OF THE ISM AND IMPLICATIONS FOR THE STAR FORMATION RATE

TINE COLMAN<sup>\* 1,10</sup>, PATRICK HENNEBELLE<sup>1</sup>, NOÉ BRUCY<sup>2,10</sup>, PHILIPP GIRICHIDIS<sup>2</sup>, JUAN D. SOLER<sup>3</sup>, SIMON C. O. GLOVER<sup>2</sup>, RALF S. KLESSEN<sup>2,4</sup>, MARC-ANTOINE MIVILLE-DESCHÊNES<sup>5</sup>, ALESSIO TRAFICANTE<sup>3</sup>, SERGIO MOLINARI<sup>3</sup>, ROWAN SMITH<sup>6,7</sup>, AND LEONARDO TESTI<sup>8,9</sup>

<sup>1</sup> AIM, CEA, CNRS, Université Paris-Saclay, Université Paris Diderot, Sorbonne Paris Cité, 91191 Gif-sur-Yvette, France

<sup>2</sup> Universität Heidelberg, Zentrum für Astronomie, Institut für Theoretische Astrophysik, Albert-Ueberle-Str. 2, 69120 Heidelberg, Germany

<sup>3</sup> INAF – Istituto di Astrofisica e Planetologia Spaziali, via Fosso del Cavaliere 100, 00133 Roma, Italy

<sup>4</sup> Universität Heidelberg, Interdisziplinäres Zentrum für Wissenschaftliches Rechnen, Im Neuenheimer Feld 205, 69120 Heidelberg, Germany

<sup>5</sup> Laboratoire de Physique de l'École Normale Supérieure, ENS, Université PSL, CNRS, Sorbonne Université, Université de Paris, F-75005 Paris, France

<sup>6</sup> Jodrell Bank Centre for Astrophysics, Department of Physics and Astronomy, University of Manchester, Oxford Road, Manchester M13 9PL, UK

<sup>7</sup> SUPA School of Physics and Astronomy, University of St Andrews, North Haugh, St Andrews, Fife, KY17 9SS, UK

<sup>8</sup> Alma Mater Studiorum Università di Bologna, Dipartimento di Fisica e Astronomia (DIFA), Via Gobetti 93/2, I-40129, Bologna, Italy

<sup>9</sup> INAF-Osservatorio Astrofisico di Arcetri, Largo E. Fermi 5, I-50125, Firenze, Italy and

<sup>10</sup> ENS de Lyon, CRAL UMR5574, Université Claude Bernard Lyon 1, CNRS, Lyon, F-69007, France

Version March 6, 2025

## ABSTRACT

What regulates star formation in different regions of the Galaxy is still debated and especially the role of turbulence is not fully understood. In this work, we explore the link between star formation, turbulence and the thermal state of the multi-phase interstellar medium (ISM). We analyse a suite of stratified box simulations modelling a realistic ISM that aims to probe environments similar to those found in the Milky Way. Turbulence is injected through stellar feedback and an external large-scale driving force. We find that star formation can be either boosted or reduced when increasing the external driving strength, depending on the environment. When the density is sufficiently high, warm neutral gas naturally transitions to the cold phase, leading to high cold neutral medium (CNM) fractions of around 40%. Under these conditions, excessive large-scale driving leads to a slight reduction of the CNM fraction and an increase in the amount of gas that is thermally unstable. What limits the star formation in this regime is a reduced fraction of dense gas due to additional turbulent support against collapse. For low density regions, overdensities in which cooling is efficient are much rarer and we find that star formation is regulated by the formation of cold gas. In such cases, turbulence can significantly boost star formation by compressing gas in shocks and increasing the CNM fraction dramatically. In our simulations we see an increase from almost no CNM to up to a fraction of 15 % when including external turbulence driving; leading to an associated increase in the star formation rate. We provide a model to quantify this behaviour and predict the CNM fraction by combining the standard ISM cooling/heating model with the density PDF generated by turbulence. The change in the dominant limiting process for star formation between low- and intermediate-density environments provides a natural explanation for the observed break in the Kennicutt-Schmidt relation around column densities of  $9 M_{\odot} \text{ pc}^{-2}$ .

*Subject headings:* ISM: structure – turbulence

## 1. INTRODUCTION

The interstellar medium (ISM) consists mainly of hydrogen gas which occurs in ionised (HII), atomic (HI) and molecular (H<sub>2</sub>) form. It has been established that HI itself has two thermal phases that coexist at the same pressure: the warm neutral medium (WNM) with temperatures of a few thousand Kelvin and the cold neutral medium (CNM) with temperatures below 250 K (Field et al. 1969; Wolfire et al. 1995, 2003; McClure-Griffiths et al. 2023). Gas in one of these two regimes is thermally stable, meaning that a small perturbation cannot change its temperature dramatically. On the other hand, gas with a temperature in the range between the CNM and WNM temperatures is thermally unstable and could undergo rapid transition to either the WNM or CNM state. This regime is called the unstable or lukewarm neutral medium (UNM or LNM).

Gas is the main raw material from which stars form. As such, relations exist between the gas reservoir and the star formation rate (SFR), which can be averaged over full galaxies or sub-

regions within, or measured for individual star-forming clouds. Schmidt (1959) proposed a power-law relation between the gas density and the SFR. The relation between the surface density, a quantity which is more directly observable especially for extra-galactic measurements, and SFR is commonly referred to as the Kennicutt-Schmidt (KS) relation (Kennicutt 1998; Kennicutt & Evans 2012). On average, it has the form  $\text{SFR} \propto \Sigma_{\text{HI}+\text{H}_2}^{1.4}$  above  $9 M_{\odot} \text{ pc}^{-2}$ , where the relation exhibits a break, and below which it shows steeper slopes and more scatter (Kennicutt 1998; Bigiel et al. 2008).

The relation becomes even more direct when considering only the molecular gas. Bigiel et al. (2008) have established a tight linear relation  $\Sigma_{\text{H}_2} \propto \Sigma_{\text{SFR}}$ , where H<sub>2</sub> was estimated from CO emission (see also Pessa et al. 2021; Sun et al. 2023). In contrast, the relation between the SFR and the HI surface density is found to vary from galaxy to galaxy (Bigiel et al. 2008; Leroy et al. 2008; Shetty et al. 2014). Since only cold gas is relevant for the formation of stars (Krumholz et al. 2009; Klessen & Glover 2016), regardless of whether it is in atomic or molecular form (Glover & Clark 2012), we would not expect a universal relation of the SFR with the total amount of HI if

\*email: tine.colman@cnrs.fr

the CNM fraction varies with environment.

Decomposition of HI into WNM and CNM is a difficult task and so far observational results are limited to the Milky Way or other Local Group galaxies (Dickey 1979; Dickey et al. 2000; HI4PI Collaboration et al. 2016; Murray et al. 2018). In their recent review, McClure-Griffiths et al. (2023) compiled an overview of CNM fraction measurements in the Galaxy. A large variety is recovered, with values ranging from zero up to 80% or more. Several trends with environment appear. Heiles & Troland (2003) found a CNM fraction that on average increases with total HI column density up to  $\Sigma_{\text{HI}} \approx 9 \text{ M}_{\odot} \text{pc}^{-2}$ , which marks the threshold between HI and H<sub>2</sub> dominated gas at solar metallicity (Bigiel et al. 2008; Leroy et al. 2008). Observations near molecular clouds typically show relatively high CNM fractions, highlighting the important connection between these two gas phases. Gas at high Galactic latitudes is found to have lower CNM fractions (Kalberla & Kerp 2009; Marchal & Miville-Deschênes 2021).

The star formation process in galaxies can thus be thought of as a sequence of steps: the condensation of CNM out of WNM followed by the possible formation of a molecular cloud out of this CNM, in which then finally dense collapsing cores form and produce stars (Schruba et al. 2011; Smith et al. 2023). Star formation can potentially be regulated through either one of these processes and the dominant limiting process is likely dependent on environment.

We know that turbulence plays a key role in star formation (e.g. Mac Low & Klessen 2004; McKee & Ostriker 2007). Observations show that molecular clouds are turbulent and its importance is now widely accepted (Roman-Duval et al. 2010; Hennebelle & Falgarone 2012; Miville-Deschênes et al. 2017). Analytical theories and simulations show that turbulence interacts with gravity in two ways. On the one hand, it widens the density PDF, creating more overdensities that may become gravitationally unstable, which is favourable for star formation. On the other hand, it provides support against gravitational collapse in the form of turbulent velocity dispersion, which reduces the rate at which dense gas is transformed into stars. These principles are the basis of the theory of turbulent fragmentation (Krumholz & McKee 2005; Padoan & Nordlund 2011; Hennebelle & Chabrier 2011; Federrath & Klessen 2012; Hennebelle et al. 2024).

It is thought that the turbulence in molecular clouds is inherited from larger scales during their formation process (Heyer & Brunt 2004; Brunt et al. 2009; Klessen & Hennebelle 2010). What exactly drives the turbulence on these scales is still debated. In present-day spiral galaxies such as the Milky Way, numerical studies indicate that stellar feedback in the form of supernova (SN) possibly in combination with ionising radiation and winds is the dominant driving mechanism in most parts of the galaxy (Peters et al. 2017; Gatto et al. 2017; Kim et al. 2020; Rathjen et al. 2021). These studies reproduce levels of star formation in agreement with observations, without needing to invoke additional limiting processes. Recently, Colman et al. (2024) investigated simulated cloud properties in different environments and from different numerical setups. They found an overall trend of the turbulent velocity dispersion consistent with large-scale turbulent decay. Furthermore, at small spatial scales – and small molecular clouds – nearby SNe leave a noticeable imprint on the velocity dispersion.

The situation may be different in the centre and outskirts of galaxies. Sun et al. (2020) showed that the velocity dispersion of clouds in the centre of barred spiral galaxies is elevated. The

same is true for the central region of our Milky Way (Shetty et al. 2012). The fact that these regions lie below the KS relation (Longmore et al. 2013), leads us to speculate that injection of turbulence from galactic dynamics plays a role here. Also in galaxies which have high gas densities, such as found at high redshift, large-scale galactic processes may be important drivers of turbulence (Krumholz et al. 2018). In their kiloparsec box simulations, Brucy et al. (2020, 2023) found that large-scale driving quenches star formation for column densities above  $20 \text{ M}_{\odot} \text{pc}^{-2}$  and that the KS relation cannot be reproduced with stellar feedback alone.

In this work, we study in more detail the effect of large-scale driving in Milky Way-like environments with column densities similar to what is found in the Solar neighbourhood. The paper is structured as follows. In Section 2, we describe the simulation setup. Our suite of eight simulations explores two values for the initial column density and various driving strengths. In Section 3, we analyse and compare the star formation activity in the different simulations. We find that, in some cases, driving can enhance star formation rather than reducing it. In Section 4, we investigate how turbulence affects the thermal balance in the simulations. Turbulence is found to influence the CNM and LNM fraction. This is then connected to the SFR in Section 5, where we take a closer look at the star formation relations. We identify two regimes, each with a different limiting process. In Section 6, we further discuss the generation of CNM through turbulence and construct the prototype of an analytical model to predict the CNM fraction. Finally, Section 7 summarises our findings and concludes the paper.

## 2. SIMULATIONS

As in previous work (Iffrig & Hennebelle 2015; Colling et al. 2018; Brucy et al. 2020), we model a  $1 \text{ kpc}^3$  region of a galaxy with realistic ISM physics. The simulations used for this work are described in Colman et al. (2022). Additionally, we include four new runs with lower initial column density, to probe a wider variety of conditions.

### 2.1. Setup

The initial condition of the simulations is a smooth, Gaussian density profile perpendicular to the mid-plane, characterised by a mid-plane particle density  $n_0$  and a thickness  $z_0 = 150 \text{ pc}$ . Our simulation suite explores two values for the initial density:  $n_0 = 0.8 \text{ cm}^{-3}$  which is equivalent to a total face-on column density of  $\Sigma = 10.2 \text{ M}_{\odot} \text{pc}^{-2}$ , and  $n_0 = 1.5 \text{ cm}^{-3}$  which corresponds to  $\Sigma = 19.1 \text{ M}_{\odot} \text{pc}^{-2}$ . We refer to these sub-sets of models as low- $\Sigma$  and high- $\Sigma$ .

We include an initial magnetic field with an orientation along the  $x$ -axis. The magnetic field strength has a Gaussian distribution in the vertical direction with the same thickness  $z_0$  as the gas and a mid-plane value  $B_0 = 7.62 \mu\text{G}$ , which is compatible with various estimates for the magnetic field in the Milky Way (Beck 2003; Heiles & Crutcher 2005; Heiles & Troland 2005).

An initial level of turbulence is introduced by adding a turbulent velocity field with a root mean square velocity dispersion of  $5 \text{ km s}^{-1}$  and a Kolmogorov power spectrum  $E(k) \propto k^{-5/3}$  with random phase. These fluctuations will kick-start structure formation. The initial temperature is uniform and set to  $5333 \text{ K}$ , which is a typical value for the warm neutral medium phase in the ISM.

## 2.2. Numerics

To evolve our simulation in time, we used the adaptive mesh refinement magneto-hydrodynamics code `RAMSES` (Teyssier 2002; Fromang et al. 2006), with treatments of the magnetic field in the ideal approximation and radiation using a moment-based method (Rosdahl et al. 2013). The simulation box is periodic in the  $x$ - and  $y$ -direction and has open boundary conditions in the  $z$ -direction. The coarse grid has a resolution of 3.9 pc and is further refined based on a mass criterion up to a maximum resolution of 0.24 pc in the densest regions. Aside from self-gravity, we also apply an external gravitational potential representing the effects of the stellar disk as prescribed by Kuijken & Gilmore (1989); Joung & Mac Low (2006). We use the ISM cooling/heating model from Audit & Hennebelle (2005) which is based on the work of Wolfire et al. (2003), further detailed in one of the next subsections. This model produces a multi-phase ISM with a warm and cold phase in our simulations, as demonstrated later on in this paper.

### 2.3. Sink particles and stellar feedback

When the gravitational collapse reaches the resolution limits, we introduce sink particles (Bate et al. 1995; Federrath et al. 2010b) according to the recipe prescribed by Bleuler & Teyssier (2014). After their birth, sinks accrete gas according to the threshold accretion scheme: gas which is above the sink formation threshold of  $10^4 \text{ cm}^{-3}$  and within the accretion radius of 4 cells will be accreted. The high- $\Sigma$  simulations have been evolved for 60 Myr during which 2 to 5 % of the gas has been converted into stars. The low- $\Sigma$  runs are computationally less demanding and have varying final times, depending on the intensity of their star formation activity.

Each time a sink has accreted  $120 M_{\odot}$  of gas, it forms an individual massive star with a mass between 8 and  $120 M_{\odot}$ , randomly drawn from the Salpeter IMF (Salpeter 1955). The remainder of the mass in the sink particle is considered to be distributed between low mass stars. The total mass of a sink is thus equal to the sum of all individual massive stars that formed in this sink, in addition to the mass of an unresolved collection of low-mass stars.

The massive stars are sources of stellar feedback. They emit ionising radiation from the position of the sink particle in which they formed and explode as a supernova at the end of their lifetime at a random location around the sink (Rosdahl et al. 2013; Geen et al. 2016; Iffrig & Hennebelle 2017; Colling et al. 2018). The supernovae inject  $4 \times 10^{43} \text{ g cm s}^{-1}$  momentum and  $10^{51} \text{ erg}$  of thermal energy, but the velocity and temperature of the surrounding gas are limited to  $300 \text{ m s}^{-1}$  and  $10^6 \text{ K}$  respectively to prevent the time step from becoming very small. For low-mass stars, the UV output is negligible and their lifetimes are much longer than the simulation time. Due to their computational cost, we do not include stellar winds. Furthermore, similar numerical studies found that radiation is more important for the regulation of the SFR and that including winds further reduces the SFR by only a factor 2 (Rathjen et al. 2021).

### 2.4. Turbulence driving

In this work, we study the effect of turbulent energy injection from large scales. This presents a source of turbulence additional to stellar feedback, mimicking the possible effect of galactic dynamical processes that occur on scales larger than the box size, such as spiral arms, a bar, or interactions with

TABLE 1  
OVERVIEW OF THE SIMULATIONS.

Group	driving	$\Sigma^a$	$n_0^b$	$f_{\text{rms}}^c$	$\sigma^d$
low- $\Sigma$	none	10.2	0.8	0	2.6
low- $\Sigma$	very weak	10.2	0.8	1500	4.8
low- $\Sigma$	weak	10.2	0.8	3000	7.4
low- $\Sigma$	medium	10.2	0.8	6000	8.3
high- $\Sigma$	none	19.1	1.5	0	8.4
high- $\Sigma$	weak	19.1	1.5	3000	9.0
high- $\Sigma$	medium	19.1	1.5	6000	12.1
high- $\Sigma$	strong	19.1	1.5	24000	20.1

<sup>a</sup>initial gas column density in  $M_{\odot} \text{ pc}^{-2}$

<sup>b</sup>initial mid-plane density in  $\text{cm}^{-3}$

<sup>c</sup>normalisation factor for the turbulence driving strength

<sup>d</sup>final velocity dispersion in  $\text{km s}^{-1}$

neighbouring galaxies. A detailed prescription of the turbulence driving can be found in Colman et al. (2022) or Bruccy et al. (2023). In short, a bi-dimensional turbulence driving force aligned with the disk plane is added as an additional stochastic external force in the Euler equation. This driving acts on scales between a full and a third of the box length and is mainly solenoidal, with a solenoidal fraction of 0.75. We explore several different forcing strengths, ranging from very weak to strong, as well as running reference simulations without external forcing (see Table 1).

In Figure 1 we compare the energy injected by large-scale driving to an estimate of the turbulence injection by SNe per unit time for each simulation. We count an energy of  $10^{51} \text{ erg}$  at an average efficiency of 6% per SN. Note that this efficiency is difficult to quantify and it depends on the environment in which the SN goes off (Martizzi et al. 2015; Iffrig & Hennebelle 2017). After an initialisation phase during which the SN rate increases, the feedback self-regulated to a fairly stable rate which is mostly dependent on the column density of the simulation. Figure 1 serves as a guide for interpreting the relevance of both driving mechanisms in the remainder of this paper.

Different forcing strengths lead to different final global velocity dispersions. In Figure 2, we show the evolution of the velocity dispersion in the different simulations, measured in the disk. This quantity reflects the differences in energy injection rate from Figure 1.

From Figure 1 and 2 we can estimate the length of the initialisation phase and after how much time the initial conditions have been washed out. For the high- $\Sigma$  runs, the SN rate is converged after 50 Myr or less. The stronger the driving, the shorter the initialisation phase. In the low- $\Sigma$  runs, the evolution proceeds slower especially when there is little turbulence.

### 2.5. Cooling and heating model

What sets the thermal balance in the ISM is a topic that has been well-studied in the past decades. Wolfire et al. (1995) summarised which processes are relevant and provide a model for the solar neighbourhood, which was later extended for other Galactic radii (Wolfire et al. 2003). More recent improvements include a more accurate treatment for low-metallicity environments (Glover & Clark 2014; Bialy & Sternberg 2019). In the context of this work, we use the ISM cooling/heating model from Audit & Hennebelle (2005). We assume solar metallicity and solar neighborhood abundances. We briefly review the dominant processes included in this model.

The dominant heating process is photoelectric heating from small dust grains and PAHs, that is the emission of elec-

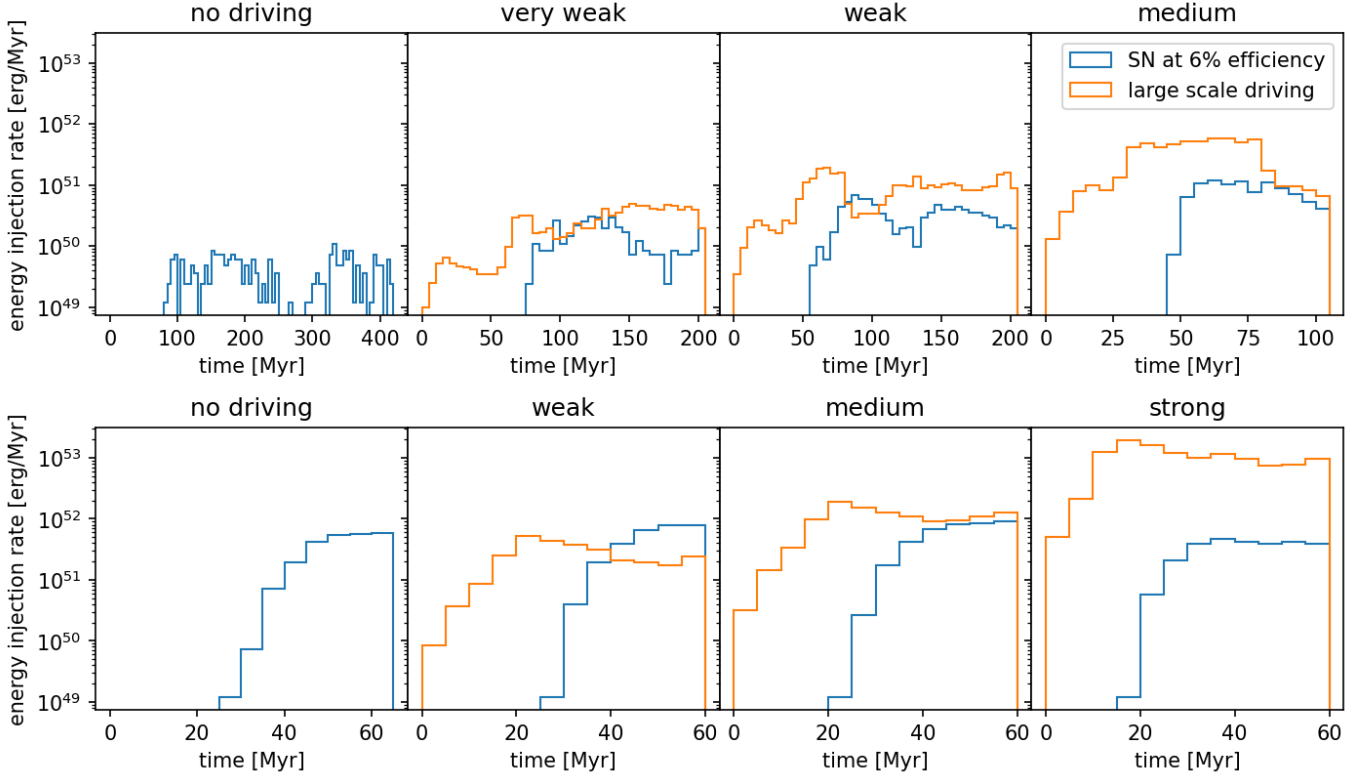


FIG. 1.— Comparison between the energy injection rate by SNe, assuming a 6% efficiency, and large-scale driving throughout the simulations averaged over bins of 5 Myr.

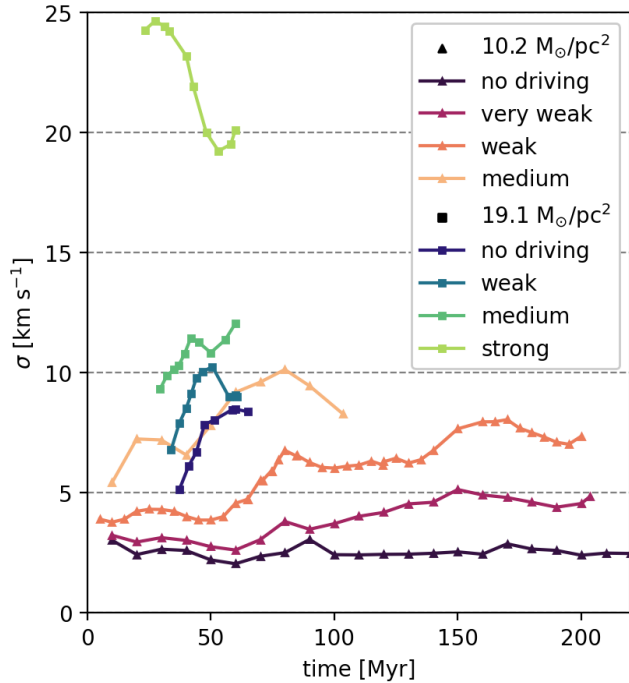


FIG. 2.— Evolution of the mass-weighted 3D velocity dispersion in the different simulations, measured in a region between 100 pc above and 100 pc below the mid-plane.

trons from the grains after exposure to the interstellar radiation field. While UV radiation can free electrons in grains of all sizes, these electrons can escape more easily from small grains. Consequently, the photoelectric heating rate depends

on the amount of small grains available and the strength of the far UV field  $G_0$ . [Bakes & Tielens \(1994\)](#) provide an analytical model as a function of  $G_0$ , the temperature  $T$  and the electron density  $n_e$ , assuming a fixed grain size distribution. Even though the photoionisation of hydrogen is followed using Ramses-RT, the electron density used in the cooling model is calculated using the formula provided by [Wolfire et al. \(2003\)](#). Corrections for photoionisation in the WNM are made based on the work of [Ferland \(2003\)](#), as is done in [Geen et al. \(2016\)](#). A constant uniform UV background with a strength equal to 0.6 Habing units is assumed ([Habing 1969](#)). In reality we expect the UV field to vary locally and to be proportional to the local SFR ([Ostriker et al. 2010](#)).

The opposite process occurs when electrons are recombined onto small grains and PAHs (e.g. [Draine 2003](#)). This process is one of the main coolants at temperatures of 8000 K and above. Together with collisional excitation of the hydrogen Ly $\alpha$  line, it keeps the temperature of the WNM roughly constant as a function of density. For temperatures below 8000 K, collisional excitation of the [CII] and [OI] fine-structure lines provides the main cooling mechanism. This implies a dependence on the abundances of carbon and oxygen in gaseous form, which are treated as constant in our simulations.

Heating sources of lesser importance are cosmic rays and soft X-rays. In this work, they are represented by a constant uniform background, but we can expect energetic events such as supernovae to boost the importance of these heating mechanisms in specific regions.

The combination of these processes sets the relation between temperature and density in the ISM. It depends on the strength of the UV field, the presence of small dust grains and PAHs, the abundances of C<sup>+</sup>, O and electrons. In reality, these can vary with the environment and change the density at which the

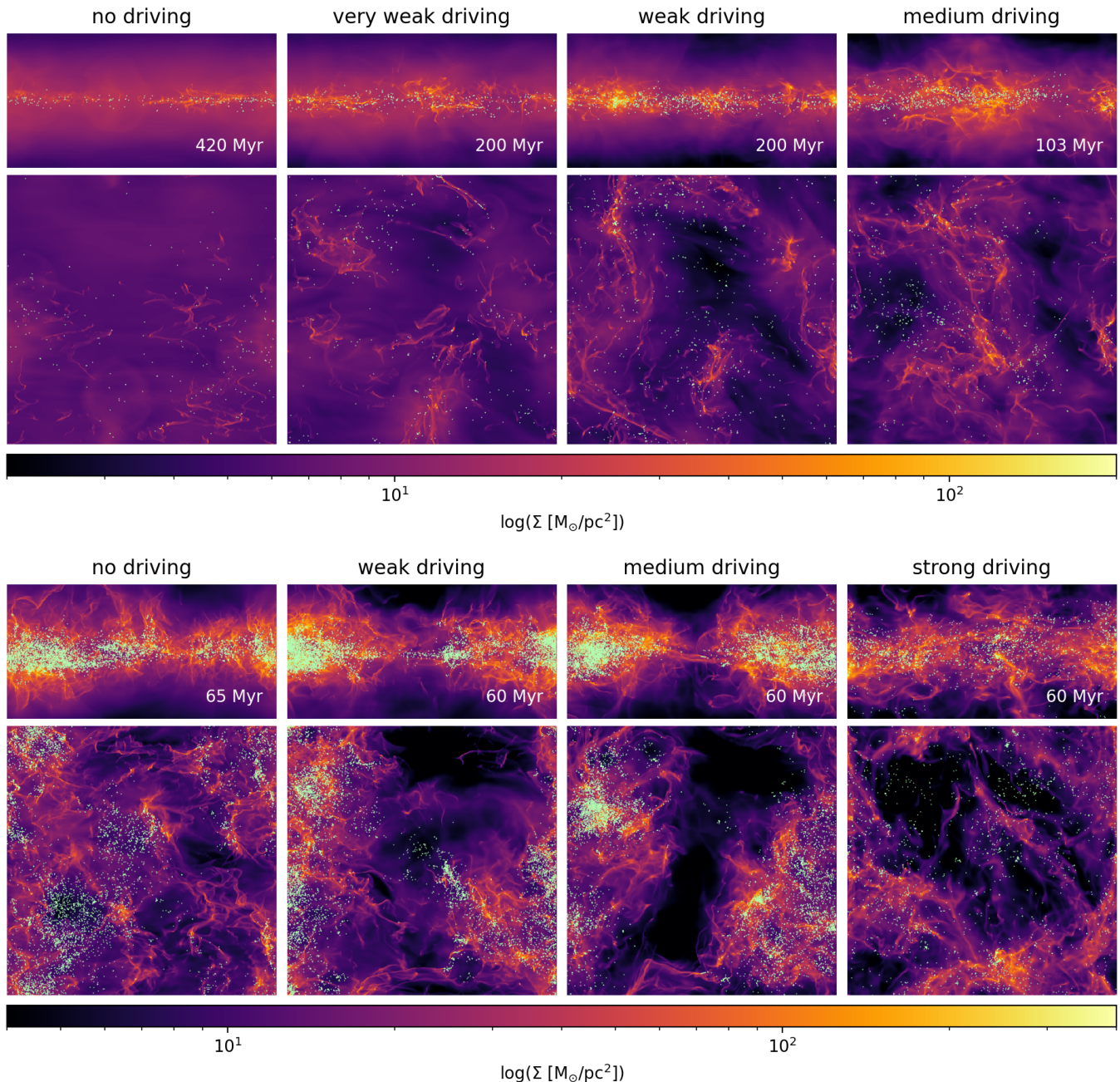


FIG. 3.— Gas surface density  $\Sigma$  for edge-on and face-on projections of the final snapshot of each simulation. The field of view is  $1 \text{ kpc} \times 0.5 \text{ kpc}$  and  $1 \text{ kpc} \times 1 \text{ kpc}$  respectively, each with a depth of  $1 \text{ kpc}$ . The green dots indicate the location of the sink particles. Top: low- $\Sigma$  runs with  $\Sigma = 10.2 \text{ M}_{\odot} \text{pc}^{-2}$ . Bottom: high- $\Sigma$  runs with  $\Sigma = 19.1 \text{ M}_{\odot} \text{pc}^{-2}$ .

transition from WNM to CNM occurs (or whether there even exists a pressure range which allows for a two-phase medium). Future simulations will include a more self-consistent coupling of cooling/heating to the propagation of radiation and ionisation treated by RAMSES-RT.

### 2.6. Simulation suite

The parameters of the different simulations are summarised in Table 1 and the final snapshot of each simulation is displayed in Figure 3. We can see a wide variety in terms of structure. The low- $\Sigma$  runs (top panels), especially the ones with no to weak driving, have a prominent diffuse gas component with a thin disk of denser material in which stars form. The high-

$\Sigma$  runs (bottom panels) are more filamentary. Increasing the driving strength leads to more large-scale structure, seen as large overdensities and voids (Colman et al. 2022).

The various simulations can be compared to different regions in the Milky Way. The low- $\Sigma$  runs could be placed in the Solar neighbourhood, or more generally at a Galactocentric radius between about 5 and 12 where the average HI column density of the Milky Way is around  $10 \text{ M}_{\odot} \text{pc}^{-2}$ . Since the chosen background UV field is lower than the Solar neighbourhood value, an inter-arm region or region beyond the solar galactocentric radius is likely more appropriate. The high- $\Sigma$  runs have column densities that are somewhat higher than what is found in most parts of the Milky Way disk. These runs may

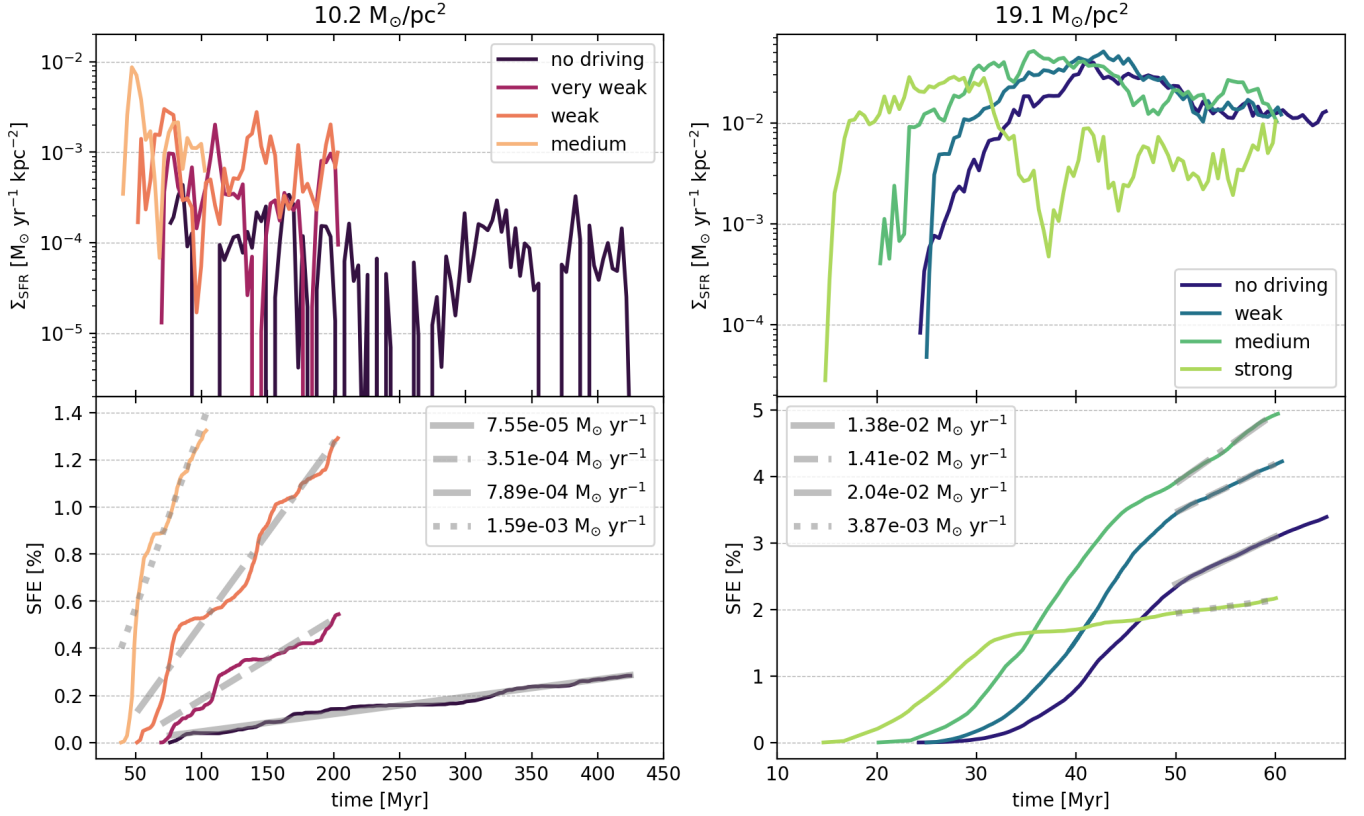


FIG. 4.— The star formation history in each simulation. Top: evolution of the star formation rate. Bottom: evolution of star formation efficiency. Left: low- $\Sigma$ . Right: high- $\Sigma$ . The grey lines show the fits to estimate the global SFR of the simulation. The labels indicate the average SFR value found from these fits.

be compared to regions that are slightly closer to the centre of the Galaxy. In this case, strong large-scale turbulence driving may mimic the effect of the central bar.

### 3. STAR FORMATION IN THE SIMULATIONS

#### 3.1. Star formation history

Using sink particles, we trace the star formation activity throughout the simulations. In the context of this work, sinks represent small star clusters rather than individual stars, and consists of a number of massive stars in addition to an unresolved collection of low-mass stars. Figure 4 displays the star formation history of each simulation. The top panels show the variation of the SFR in time, which exhibits large fluctuations. The bottom panel shows the evolution of the SFE, defined as the amount of gas which is in sinks compared to the total mass available at the beginning of the simulation. The general behaviour is different for the low- $\Sigma$  runs ( $10.2 \text{ M}_\odot \text{ pc}^{-2}$ , left panels) compared to the high- $\Sigma$  runs ( $19.1 \text{ M}_\odot \text{ pc}^{-2}$ , right panels) and we see two regimes emerge.

For the low- $\Sigma$  simulations, large-scale turbulence driving boosts star formation. Both the SFR and SFE increases significantly with increasing driving strength. Without driving there is overall little star formation activity and there are epochs where there is no star formation at all. Consequently, there is also little turbulence injection by stellar feedback (Figure 1). In all cases, the evolution consists of a sequence of alternating bursts and quiescent phases, resulting in a characteristic staircase pattern in the SFE evolution. Even in the no-driving case we recover this pattern, though the amplitude of the bursts is much lower. Increasing the driving strength increases the intensity of the bursts and shortens the length of quiescent

phases.

In the high- $\Sigma$  runs, we see that weak and medium driving boost the overall SFE compared to the case without external driving. The SFR at the end of the simulation is similar between the no-driving, weak and medium driving cases. For strong driving however, we see a significant decrease in both SFR and SFE. These runs demonstrate the duality of turbulence: adding a weak to moderate amount of turbulence slightly enhances star formation, but cranking up the driving strength too much leads to quenching. We also note that star formation starts earlier when we increase the driving strength. Since we start from a smooth density profile, cold gas structures have to be generated from scratch by the velocity perturbations. The additional external turbulence helps to kick-start cloud formation. This is followed by a first phase of accelerating star formation, during which stellar feedback establishes its role in the SFR regulation. Note that this phase is shorter for the strong driving case. After the initialisation period, the evolution of the SFE becomes linear, indicating a roughly constant SFR, as opposed to the bursty nature seen at lower  $\Sigma$ . Possibly, a similar staircase pattern would emerge if the simulations were evolved for a longer time.

The qualitative findings described here for modest column densities are different from the results obtained for column densities above  $20 \text{ M}_\odot \text{ pc}^{-2}$ , where large-scale driving was found to always reduce the SFR (Brucy et al. 2020, 2023). This indicates that the relative importance of the processes involved in star formation varies with the column density of the region.

#### 3.2. Global SFR

We can obtain an overall SFR for each simulation by fitting a linear function to the SFE evolution in the appropriate time frame. For high- $\Sigma$ , we choose the range between 50 and 60 Myr where all simulations are in the linearly increasing SFE regime. We find values of  $1.4 \times 10^{-2} M_{\odot} \text{yr}^{-1}$  for no-driving and weak driving,  $2.0 \times 10^{-2} M_{\odot} \text{yr}^{-1}$  for medium driving and  $0.39 \times 10^{-2} M_{\odot} \text{yr}^{-1}$  for strong driving, i.e. a reduction of roughly a factor 4 compared to the others. To determine the value for the SFR in the low- $\Sigma$  regime, we simply fit the SFE over the entire time range from the moment the first stars form, averaging over bursts and quiescent phases. We obtain a value of  $7.6 \times 10^{-5} M_{\odot} \text{yr}^{-1}$  for the no-driving case,  $3.5 \times 10^{-4} M_{\odot} \text{yr}^{-1}$  for very weak driving,  $7.9 \times 10^{-4} M_{\odot} \text{yr}^{-1}$  for weak driving and  $1.6 \times 10^{-3} M_{\odot} \text{yr}^{-1}$  for medium driving. Here, the SFR increases with driving strength and the additional turbulence can boost the SFR by more than an order of magnitude.

#### 4. THERMAL STATE OF THE GAS

In the previous section, we showed that turbulence can either boost or reduce the SFR, depending on the global conditions of the simulation box. To gain insight into this behaviour, we turn our attention to the thermal state of the two-phase ISM.

##### 4.1. Gas phases

In Figure 5, we show the phase diagram of all the gas (neutral and ionised) in a snapshot of the low- $\Sigma$  simulation with weak driving. For the other simulations, the diagram look qualitatively similar. It shows the relation between density and temperature or pressure, as well as the mass weighted histogram of each of those quantities. The pressure versus density diagram exhibits the characteristic S-shape with the WNM as the left diagonal branch and the CNM as the right diagonal branch. In between sits the LNM, which connects the two states. Both the warm and cold medium exist in the same pressure range. The typical ISM pressure is around  $3 \times 10^{-13} \text{ erg cm}^{-3}$ .

On the density-temperature diagram we overlay the theoretical curve given by the cooling model as a dashed black line. The WNM has a temperature between 3000 and  $10^4$  K. Two distinct WNM branches with each their characteristic temperature are visible: one at  $T \approx 4500$  K ( $\log T = 3.65$ ) and the other at  $T \approx 8000$  K ( $\log T = 3.90$ ). In the appendix, we show that these can be associated to different levels of ionisation. The lower temperature branch corresponds to partially ionised gas (between 0.5 % and 50%). This is likely a numerical artefact caused by inconsistencies in the treatment of cooling and ionisation, as noted in Section 2.5. From a density of about  $1 \text{ cm}^{-3}$ , the temperature drops as the gas becomes thermally unstable until it reaches CNM temperature of 250 K and below. The characteristic CNM temperature is between 30 and 100 K.

In the density PDF (top panel), the WNM and CNM phases can be identified as distinct bumps around a characteristic density of about  $0.5 \text{ cm}^{-3}$  and  $30 \text{ cm}^{-3}$  respectively. Note however that not all dense gas is cold. Dense shells around newly formed stars are heated and partially ionised by the UV radiation emitted by those stars. This makes photoelectric heating more efficient and brings the gas to WNM temperatures. Further investigation of this phenomenon requires more careful coupling between photoelectric heating, ionisation and the propagation of the local UV field in the simulations, which is beyond the scope of this work.

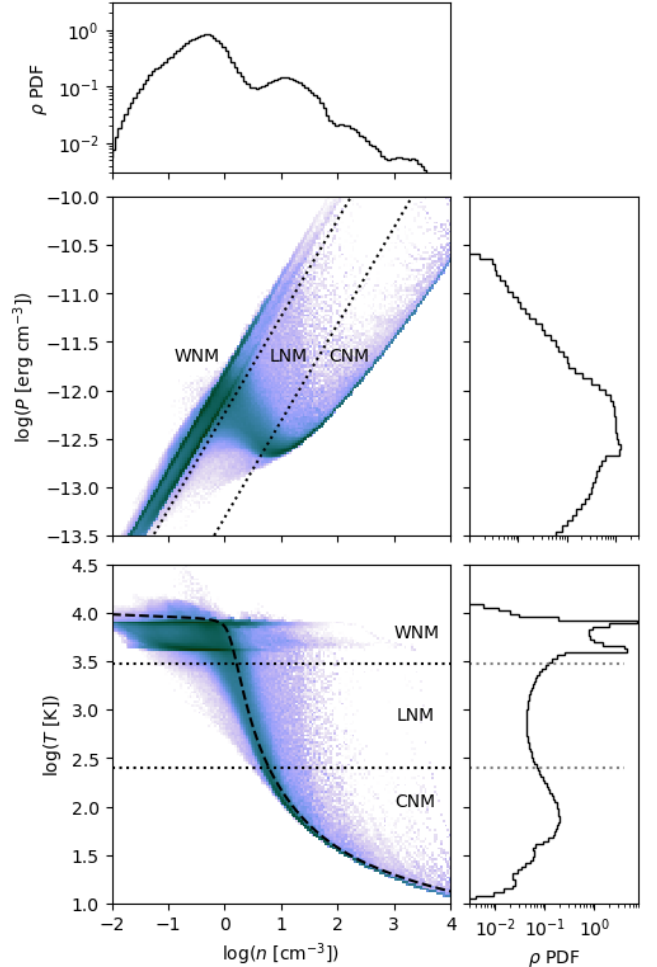


FIG. 5.— An example of a phase diagram, which show the relation between pressure  $P$  or temperature  $T$  and number density  $n$  in the simulations. The colour corresponds to the mass fraction, on a logarithmic scale, with dark being high and light being low. We also show the mass-weighted histograms of each quantity. The dashed black line shows the theoretical cooling model, while the dotted lines indicate the temperature thresholds we adopts for the definition of WNM and CNM in this work.

In what follows, we will adopt the following definitions for the gas phases. Neutral gas with a temperature below 250 K is considered to be CNM. This threshold temperature is in agreement with the one used in observations (McClure-Griffiths et al. 2023). Note that this definition also includes molecular hydrogen, which is expected to form from cold gas at high densities but whose formation is not tracked explicitly in these simulations. For the lower bound on the temperature of the WNM we choose 3000 K, a value slightly below what is proposed in McClure-Griffiths et al. (2023), to include our lower temperature WNM branch. The LNM is then everything with temperatures in between these thresholds. Our boundaries are shown as dotted lines in Figure 5.

##### 4.2. Fraction of gas in each phase

We quantify the fraction of neutral gas that is in each thermal phase. In Figure 6, we show how the CNM and LNM fractions evolve over time in all runs. The WNM fraction is simply  $1 - f_{\text{CNM}} - f_{\text{LNM}}$ .

For low-density environments, large-scale turbulence driving significantly promotes the formation of cold material, seen as an increase in both the CNM and LNM fraction. Without

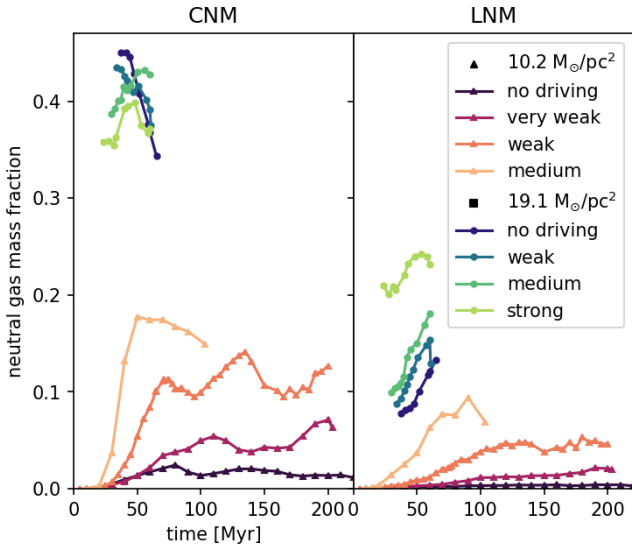


FIG. 6.— Evolution of the CNM and LNM mass fractions in full and empty circles respectively.

driving, there is almost no CNM, nor LNM. Turbulence driving thus triggers thermal instability and sets in motion the conversion from WNM to LNM to CNM. The stronger the driving, the larger the increase in CNM fraction. There is up to an order of magnitude more CNM in the driving runs compared to no driving.

For the high-density regions on the other hand, the CNM is less affected by the external driving. The CNM fraction is generally larger than in the low- $\Sigma$  runs, around 40%. This indicates that the *external* driving is not the dominant mechanism for creating CNM here. However, possibly turbulence injected by *stellar feedback* plays a similar role. Alternatively, the thermal transition occurred spontaneously due to the larger average density.

We also note important differences in the LNM fraction: driving increases the LNM fraction for all simulations. Notably for the high- $\Sigma$  runs, the ratio of  $f_{\text{CNM}}/f_{\text{LNM}}$  decreases. Driving keeps more gas in the thermally unstable phase, possibly preventing the formation of more CNM or reheating the CNM that was formed before. This effect could potentially be used to constrain the level of turbulence in galaxy simulations where the turbulence driving strength in sub-regions is not controlled. Perhaps this relation can also be used to find signatures of turbulence driving in observations, although it remains challenging to observationally quantify the neutral gas phase fractions.

#### 4.3. Dense gas

While stars are found to form mainly in molecular clouds, only the densest parts of these clouds are actively star-forming. Figure 7 shows a cumulative distribution function of the density, quantifying how much of the gas is above a certain density. We normalised the curves using the total mass in the simulation.

For the low- $\Sigma$  runs, the large differences in the amount of CNM are again visible here as the curves start to diverge above about  $0.5 \text{ cm}^{-3}$ , the density where the WNM becomes thermally unstable. This difference propagates to larger densities and only a few percent of the LNM+CNM gas reached densities beyond  $100 \text{ cm}^{-3}$ .

The situation is different for the high- $\Sigma$  runs, which all have

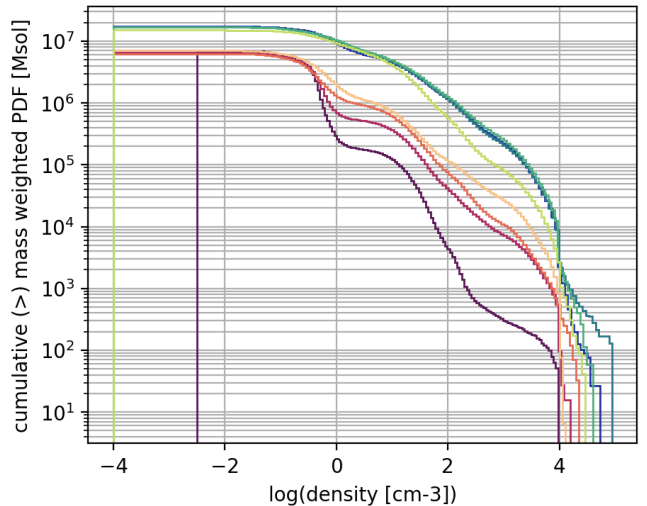


FIG. 7.— Cumulative distribution function of the density, in absolute mass units for a representative snapshot of each simulation. The simulations are colour-coded as in Figure 6.

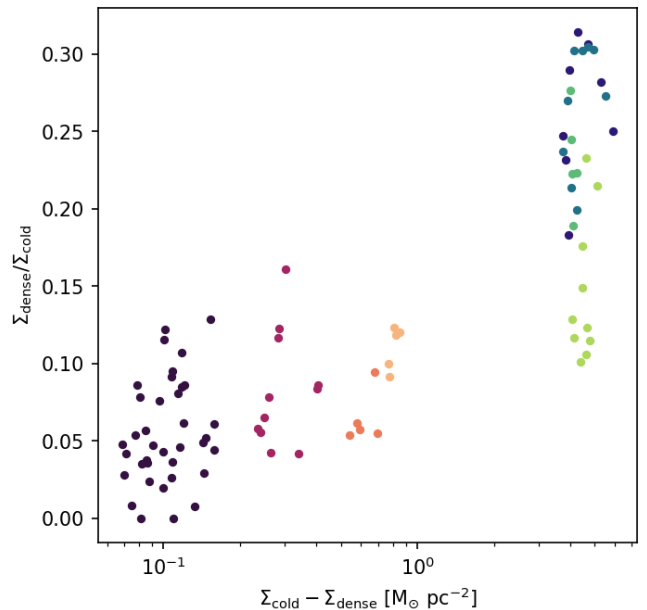


FIG. 8.— The efficiency of the conversion of cold into dense gas, quantified as the fraction of cold gas which has a density higher than  $100 \text{ cm}^{-3}$ . The x-axis is the column density of the low-density CNM ( $n_{\text{CNM}} < 100 \text{ cm}^{-3}$ ). The simulations are colour-coded as in Figure 6.

a similar cumulative density distribution up to about  $10 \text{ cm}^{-3}$ , at which point the strong driving run starts to deviate from the other three runs. In the case of strong driving, there is significantly less gas with densities above  $100 \text{ cm}^{-3}$ .

We further quantify the efficiency of the formation of dense gas in cold clouds in Figure 8, where we plot the ratio between the amount of CNM versus the amount of gas with densities greater than  $100 \text{ cm}^{-3}$ . For a point in the bottom left part of the diagram, the amount of cold material is small and the conversion to high density gas is inefficient. If a point is in the top part of the diagram, it means the conversion to dense gas is efficient. In the low- $\Sigma$  regime the conversion from cold to dense gas occurs at a roughly equal, albeit low, efficiency which is independent of the level of externally driven turbu-

lence. While the amount of cold HI is similar for all high- $\Sigma$  runs, there is about a factor 2 to 3 less dense gas for the strong driving case. This brings the efficiency to the levels of the lower column density simulations. Strong driving hinders the creation of dense self-gravitating clumps. This is in line with predictions by analytical theories of gravo-turbulent fragmentation (Hennebelle & Chabrier 2008; Hennebelle et al. 2024).

#### 4.4. A dual role of turbulence on the thermal state?

It is already established that turbulence has a dual nature with respect to gravity. On the one hand, it generates local overdensities which are the seeds of gravitationally unstable clumps. On the other hand, it provides additional support under the form of turbulent kinetic energy against this exact same gravitational collapse. This effect is seen in the high- $\Sigma$  runs where strong driving significantly reduces the fraction of dense gas.

Here we demonstrated that turbulence possibly has a second, thermal, dual nature which typically occurs at larger scales. Hennebelle & Pérault (1999) already showed that turbulence can create cold condensations in the ISM. Here, we saw that it acts as a perturbing force, promoting phase change and moving the gas away from thermal equilibrium, seen by a consistent increase in LNM fraction (Figure 6). The duality then lays in the creation versus destruction of CNM. Our simulation results seem to indicate turbulence has a stronger impact on the WNM-to-CNM conversion than on the reverse conversion. In fact, there is no indication that turbulence is able to bring the gas back into the WNM state, as the WNM fraction decreases and more gas is in the unstable regime. However, we have to keep in mind that turbulence is not only driven by the external large-scale force that is applied during the simulation. Stellar feedback also drives turbulence. For the set of high- $\Sigma$  simulations, the turbulent energy injection by SN is either stronger or comparable to that of the large-scale driving, except for the run with strong driving (Figure 1). Furthermore, the SFR in those three runs is similar, so only in the case of strong driving would we be able to directly link a change in the gas-phase fractions to an excess of turbulence. If the level of turbulence is a determining factor for CNM formation, we would expect the three other simulations to have similar CNM fractions, as is indeed the case. Possibly the stellar feedback self-regulated the WNM and CNM fractions. Controlled simulation of a multi-phase ISM without stellar feedback, could help quantify the dual role of turbulence on the CNM fraction further. Note that the role of feedback is more complex than just injecting turbulence, as massive stars emit UV radiation which contributes directly to the heating of the ISM.

#### 4.5. Caveats of the simulations

The transition point between WNM and CNM depends on the UV radiation field, metallicity and hydrogen ionisation rate (Wolfire et al. 2003). While our simulations do track the local UV photon field which is used to determine the ionisation of the gas, this information is not used in the cooling model where a uniform background UV field fixed to the solar neighbourhood value  $G_0$  is assumed. Observations in the Milky-Way and nearby galaxies show that the UV field strength decreases as a function of galactic radius. The UV field in our low- $\Sigma$  runs may thus be too high compared to real low density regions in galaxies. A lower UV field implies less heating which would lead to naturally higher CNM fraction. Furthermore, in the majority of environments we expect the

UV field to be directly coupled to the formation of new stars, especially massive ones. Test simulations where the uniform UV background is proportional to the SFR according to the recipe of Ostriker et al. (2010), indeed result in more structure formation and enhanced SFRs compared to the low- $\Sigma$  runs presented here. It is however unclear how *local* variations in the UV field may affect the overall CNM fraction. While we demonstrated a clear influence of turbulence under a fixed UV field, in practice regions with conditions similar to those in the low- $\Sigma$  runs may be rare.

Our simulations also do not take into account complex galactic effects such as differential rotation or the presence of spiral arms.

## 5. STAR FORMATION RELATIONS

In section 4 we have investigated the effect turbulence driving has on the amount of cold gas and dense gas. In this section, we link changes to these mass reservoirs to changes in star formation activity.

### 5.1. SFR versus different gas phases

As discussed in the introduction, observations have revealed correlations between the gas surface density and the SFR. In Figure 9 we correlate the SFR with different gas reservoirs in the simulations. The SFR is measured over time intervals of 0.1 Myr. Observations usually distinguish between HI and H<sub>2</sub>, the later estimated from CO emission. Our simulations do not track chemical evolution and it is non-trivial to estimate the fraction of the neutral gas which would be H<sub>2</sub>. Instead, we will simply separate the dense gas component, that is cold gas with densities exceeding  $n_{\text{neutral}} > 100 \text{ cm}^{-3}$  as in Section 4.3.

In the left panel of Figure 9, we show the total neutral gas versus the SFR. We compare with the observational results from Bigiel et al. (2008), who studied the KS-relation in a sample of 18 galaxies. Their results for HI + H<sub>2</sub> are shown as contours, where the outer contour sketches the full extend of their data points and the inner contour indicate where most of the measurements are situated. The observations are characterised by a break at  $9 M_{\odot} \text{ pc}^{-2}$ . For higher column densities, a power-law relation with index 1.4 is found, while for lower column densities the relation is steeper with a lot of scatter (Kennicutt & Evans 2012). The results from the high- $\Sigma$  runs fall in the observed range, though the SFR might be a bit high compared to the majority of the observations. Possibly this is because we do not include early feedback in the form of stellar winds and jets, which are expected to reduce the SFR by a factor 2 (Rathjen et al. 2021; Verliat et al. 2022). At low column density, we reproduce the large scatter. The simulations without driving produce SFRs which are below the observed range. This could mean that the environment modelled by this simulation is unlikely to occur in real galaxies. Indeed, large-scale dynamic effects such as rotation or infall would provide a minimal level of turbulence driving. The simulations with strongest driving (orange and green points) generally agree best with the observations.

The middle panel shows the relation with cold gas, that is CNM and cold dense gas which would be molecular. A positive correlation now appears at low column densities. These findings are in line with the results from Smith et al. (2023) who studied the distribution of CNM in their full galaxy simulation. Overall, the relation between the column density of cold gas and the SFR exhibits a scatter of about one order of magnitude around a power-law with index 1.4. This is the same index as found for the relation with total gas, above a

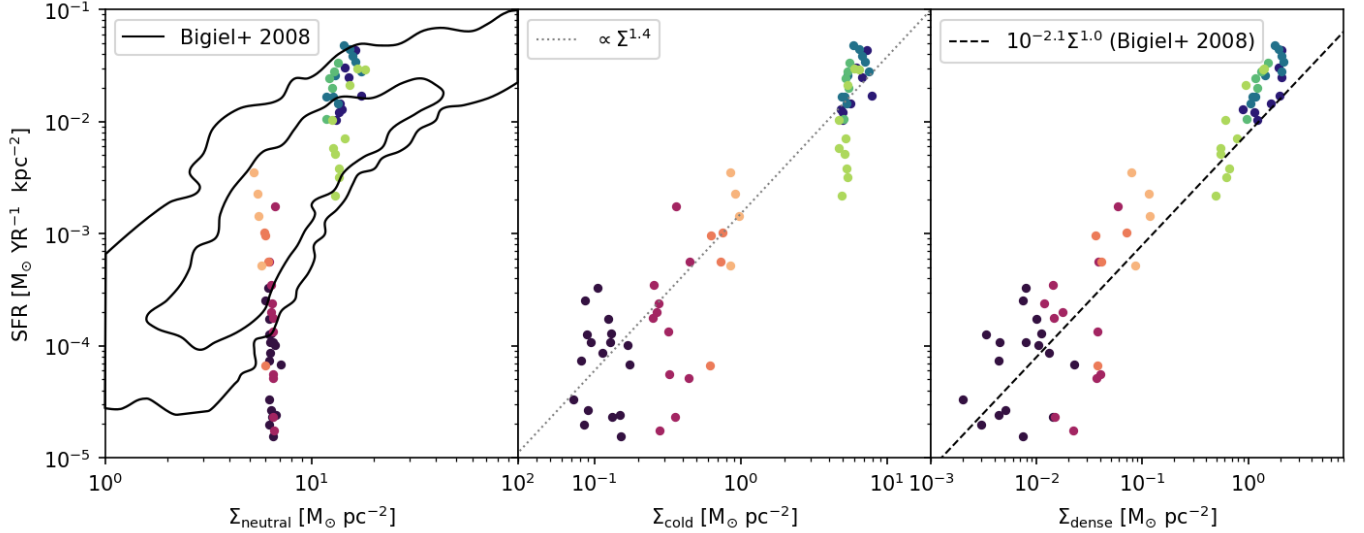


FIG. 9.— Relations of the SFR with column density for different gas reservoirs. In the left panel, the contours sketch the location of the data point from Bigiel et al. (2008): the outer contour tracers roughly all points, while inner one corresponds roughly to their orange contours denoting 2 independent data point per 0.05 dex. In the middle panel, we show a power-law with index 1.4 to guide the eye. In the right panel, we show the linear relation found by Bigiel et al. (2008) between the SFR and the column density of  $\text{H}_2$  gas, and extrapolate to lower densities. The simulation data is colour-coded as in Figure 6.

column density of  $20 \text{ M}_\odot \text{pc}^{-2}$ . This leads us to the conclusion that the scatter in the observations of the KS-relation at low column densities, as shown in the left panel, is likely due to regional differences in the CNM fraction. Following this line of thought, it implies that at higher column densities the CNM fraction on a scale of 1 kpc does not vary significantly between regions. Indeed, in the simulations we find it to be around 40% independent of the external driving strength.

Finally, the right panel shows the relation of the SFR with the dense, cold gas. As expected, we find a good correlation especially at higher densities. We compare with the linear relation between SFR and  $\text{H}_2$  found by Bigiel et al. (2008) and extrapolated to lower column densities and find good agreement. That the agreement extends to the normalisation of the relation may be fortuitous. The linearity of the relation is however not a coincidence, as many other studies confirm the existence of a linear relation between dense gas and star formation (Lada et al. 2010; Elia et al. 2022).

### 5.2. Knee-density of the KS-relation: two regimes

The kink in the KS-relation is observed around  $9 \text{ M}_\odot \text{pc}^2$ , in between the low- and high- $\Sigma$  runs. The findings from our simulations suggest this marks a transition between two regimes of star formation, each with a different dominant limiting process.

In the low density regime, we find a correlation between the amount of CNM and the SFR. In this regime, star formation is regulated predominantly by the formation of cold clouds. This in turn is set by the complex balance of cooling and heating processes in the ISM, which depend on environmental conditions such as the strength of the UV field and the metallicity of the gas. Additionally, we found that turbulence can boost the CNM fraction in this regime, due to its ability to generate overdensities in which cooling is more efficient. Low density regions exposed to an external form of turbulence driving would thus have increased CNM fractions and SFRs compared to unperturbed regions. The increased amount of cold gas gives rise to an increase in the amount of dense gas which, in turn, is directly and linearly proportional to the SFR. These environmental dependencies for CNM formation lead

to large scatter in the KS-relation at low density.

In the high- $\Sigma$  regime, CNM fractions are naturally higher since the densities at which cooling is efficient are reached more easily, leading to an abundance of cold clouds. Even though we found small variations in the CNM due to excessive turbulence driving, these could not explain the reduction by a factor 4 of the SFR in the run with strong driving. In this regime, star formation is limited by the formation of dense clumps inside cold clouds rather than the formation of the clouds themselves. The role of turbulence changed, as excessive turbulence provides additional support against gravitational collapse and reduces the amount of dense gas available for star formation.

From our simulations, it is not clear whether turbulence still plays an important role in the creation of cold clouds at high densities. We saw that strong external driving keeps a significant amount of the gas in the thermally unstable phase. Stellar feedback also injects turbulence and so a certain minimum level of turbulence driving can be associated to a SFR. Together with the additional UV heating of young stars, this may lead to a self-regulation of the CNM-fraction on kpc scales in regions with  $\Sigma > 9 \text{ M}_\odot \text{pc}^2$ .

## 6. MODEL FOR TURBULENCE INDUCED CNM FORMATION

The simulation results indicate that turbulence can trigger the cooling of gas initially in the WNM state, and that this may be an important regulator for star formation in the low density regions. The mechanism behind this is similar as for the balance of turbulence with gravity: turbulence creates overdensities. Since cooling is efficient in high density gas, overdensities created by shocks cool fast to the CNM state.

While many numerical studies have investigated structure formation in a turbulent multi-phase ISM (Audit & Hennebelle 2005; Hennebelle et al. 2007; Walch et al. 2011; Seifried et al. 2011; Saury et al. 2014; Walch et al. 2015; Kim & Ostriker 2017; Colman et al. 2024), an analytical model that described the interaction of turbulence with the thermal state of the gas is still lacking. Here, we propose such a model with the aim of predicting the CNM fraction. The general idea is to integrate the mass-weighted density PDF of a turbulent

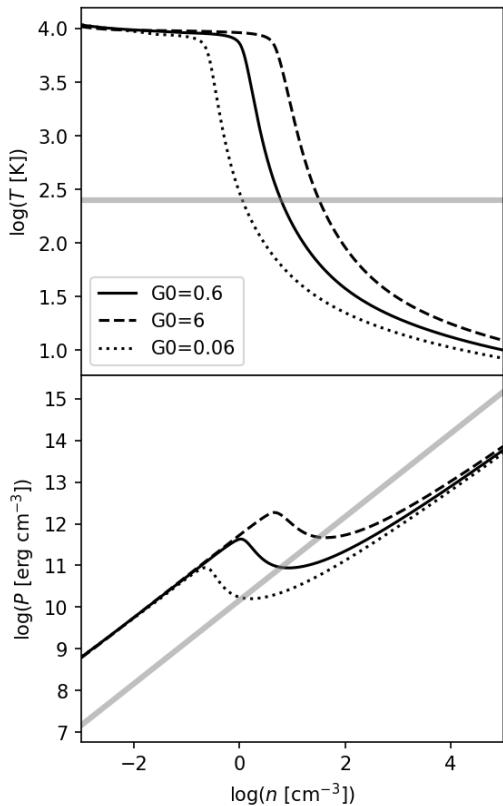


FIG. 10.— Theoretical temperature-density and pressure-density curve obtained from the cooling model of [Wolfire et al. \(2003\)](#), as described in Section 2.5, for different values of the UV field strength  $G_0$ . The gray line indicates the chosen temperature threshold for CNM.

two-phase ISM above a threshold density derived from the temperature-density curve predicted by the cooling/heating model.

### 6.1. General assumptions

We assume that turbulence is the dominant source of density fluctuations and thus the main mechanism for CNM creation. This assumption may not be valid in regions with strong gradients in the gravitational potential. We do not specify the source of turbulence, which could be for example stellar feedback and/or large-scale galactic processes. The strength of the turbulence is considered to be a free parameter and a characteristic of the environment. It can depend on the level of star formation and whether the region is subject to large-scale galactic processes.

We do not take into account that CNM formation will lead to star formation which is associated with an increase in UV field strength, ionisation and heating ([Ostriker et al. 2010](#)). This could potentially contribute to self-regulating the CNM fraction.

As in the simulations, we only consider the case of solar metallicity gas and solar neighbourhood abundances for the dominant coolants. Other metallicities can be explored by adapting the cooling/heating prescription on which the model is build.

### 6.2. Heating/cooling model and threshold density

We use the cooling/heating model from [Wolfire et al. \(2003\)](#) described in Section 2.5. The combination of processes leads to the curves shown in Figure 10. The only parameter we vary

here is the UV field strength  $G_0$ . A strong UV field will boost photoelectric heating and move the WNM – CNM transition to higher densities, while leaving the shape of the curve relatively unchanged.

To determine the threshold density  $n_{\text{thr}}(G_0)$ , we could calculate at which density the sign of the derivative  $dP/dn$  changes. The first change, from positive to negative, marks the transition from WNM to LNM. The second change, from negative to positive, is associated with the transition from LNM to CNM. Here, we simply impose the same temperature thresholds as used to define the phases in the simulation, 3000 K and 250 K, and determine numerically to which density this corresponds. The 250 K threshold for CNM formation is marked with a gray line in Figure 10. It agrees well with the bend in the pressure-density curve.

### 6.3. Density PDF generated by turbulence

It is well-established that turbulence generates log-normal-like density PDFs in isothermal media and that the Mach number controls the width of the distribution ([Federrath et al. 2008, 2010a](#)), as highly turbulent regions contain stronger density fluctuations. As a function of the density contrast  $\delta = \ln(n/n_0)$ , where  $n_0$  is the average number density of the region, the density PDF of a turbulent isothermal medium can be described by

$$\mathcal{P}(\delta) = \frac{1}{\sqrt{2\pi S}} \exp\left(-\frac{(\delta - \bar{\delta})^2}{2S}\right) \quad (1)$$

with

$$S = \ln\left(1 + b^2 \mathcal{M}^2\right) \quad (2)$$

$$\bar{\delta} = -S/2, \quad (3)$$

For the compressibility factor  $b$ , we assume the value of 0.5 for a natural mix of solenoidal and compressive modes.  $\mathcal{M} = \sigma/c_s$  is the Mach number, with  $\sigma$  the 3D velocity dispersion generated by the turbulence and  $c_s$  the sound speed in the medium.

### 6.4. Modified density PDF of a two-phase ISM

The sound speed in the neutral ISM depends on the temperature

$$c_s = \sqrt{\frac{k_B T}{1.4 m_p}}, \quad (4)$$

where 1.4 is the molecular weight of a mixture of atomic hydrogen and helium. The ISM is however not isothermal. Due to the temperature difference, the sound speed in the WNM is typically about a factor 10 larger than in the CNM. As a result, the Mach number of the WNM is smaller than that of the CNM.

Instead of choosing one constant sound speed to calculate the Mach number that regulates the width of the density PDF, we explicitly take into account the dependence of the temperature. Using the relation between temperature and density dictated by the heating/cooling model, shown in Figure 10, this temperature dependence transforms into a density dependence. This effectively makes  $S$  density dependent. Writing this explicitly, we obtain

$$S(n) = \ln\left(1 + b^2 \frac{1.4 m_p \sigma^2}{k_B T(n)}\right). \quad (5)$$

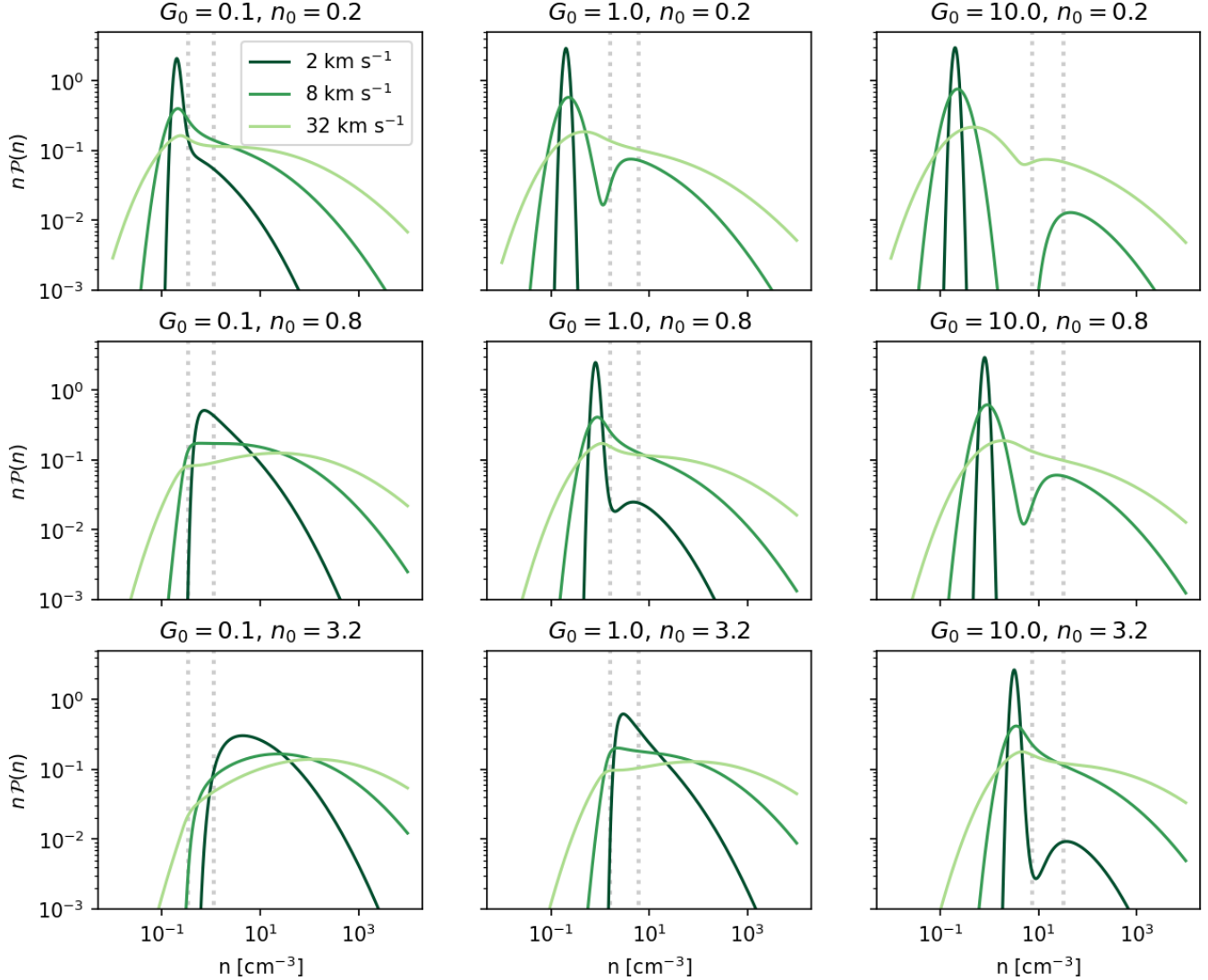


FIG. 11.— Model for the mass-weighted density PDF of a turbulent two-phase ISM subject to the relation between temperature and density shown in Figure 10. The parameter dependence on UV field strength  $G_0$ , average density  $n_0$  and 3D velocity dispersion  $\sigma$  in km/s is explored. The dotted lines mark the densities corresponding to the boundary temperatures, 3000 K and 250 K, used to separate the WNM, LNM and CNM phases.

Note that this implicitly also adds a dependence on  $G_0$ , which we consider constant here. We assume that  $\sigma = \sigma_{\text{WNM}} = \sigma_{\text{CNM}}$ , which may not be the case.

Replacing Eq. (2) by Eq. (5) results in a density PDF with a more complex dependence on  $n$ , as shown in Figure 11 for a variety of values for the parameters  $\sigma$ ,  $n_0$  and  $G_0$ . Interestingly, in most configurations we reproduce a bimodal shape similar to the one seen in the density PDF of the simulations (Figure 5). This is due to the combination of the low Mach number WNM which produces a narrow log-normal component, with a higher Mach number CNM described by a broader distribution.

The narrow WNM peak is most pronounced when  $G_0$  is high or  $n_0$  is low. Under these conditions, the WNM is the dominant phase. On the other hand, when  $n_0$  is high and  $G_0$  low, the broad CNM distribution is dominant and the WNM peak barely noticeable. Both components broaden with increasing levels of turbulence, now quantified directly through  $\sigma$  rather than  $\mathcal{M}$ .

The relative importance of the broad versus the narrow com-

ponent sets the CNM fraction. The model qualitatively captures the behaviour observed when increasing the external driving strength in the low- $\Sigma$  simulations: when  $\sigma$  increases, the WNM peak becomes less pronounced, while the opposite happens for the broad CNM contribution.

#### 6.5. Parameter dependence of the predicted CNM fraction

To obtain the CNM fraction  $f_{\text{CNM}}$  in a region of turbulent ISM characterised by  $\sigma$ ,  $n_0$  and  $G_0$ , we integrate the modified mass-weighted log-normal density PDF above the CNM density threshold:

$$f_{\text{CNM}} = \frac{1}{N} \int_{n_{\text{thr}}(G_0)}^{\infty} \mathcal{P}(n, n_0, \sigma) n dn, \quad (6)$$

where  $N$  is a normalisation factor such that  $0 \leq f_{\text{CNM}} \leq 1$ ,

$$N = \int_0^{\infty} \mathcal{P} n dn. \quad (7)$$

The resulting CNM fraction and its dependence on  $\sigma$ ,  $n_0$  and  $G_0$  is illustrated in Figure 12.

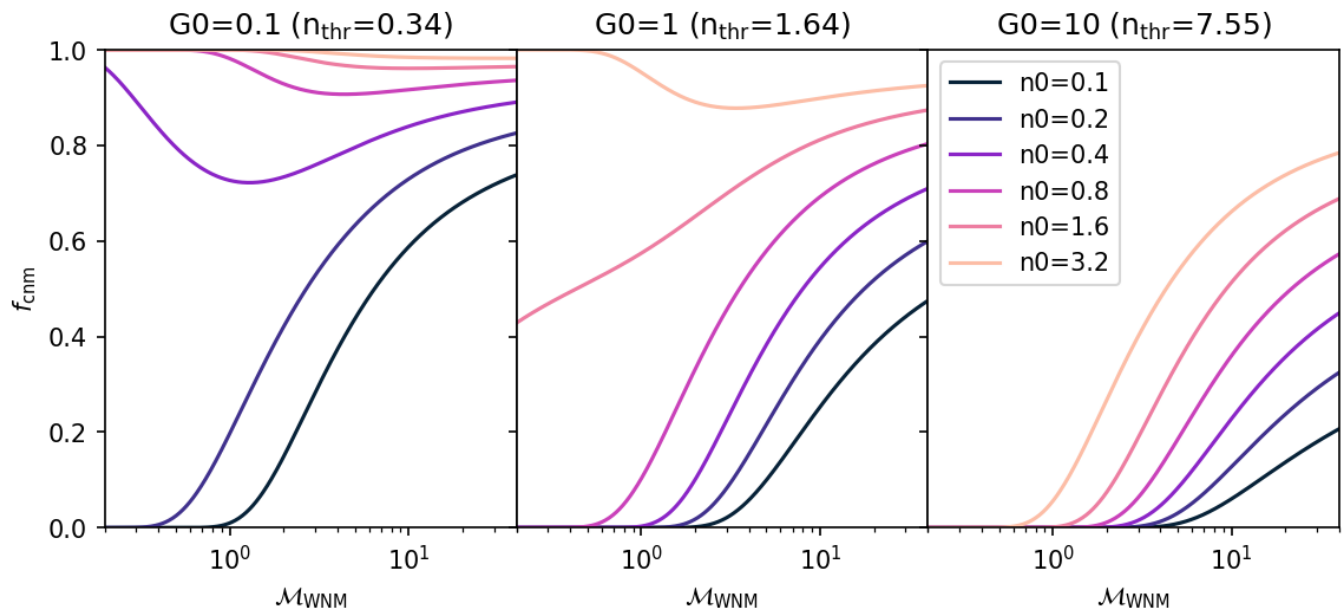


FIG. 12.— Parameter dependence of the CNM fraction model.

The behaviour of  $f_{\text{CNM}}$  with increasing  $\sigma$  depends on how the average density compares with the CNM threshold density. If  $n_0 < n_{\text{thr}}$ , the CNM fraction is zero at low levels of turbulence and increases steadily with  $\sigma$ . When  $n_0 \approx n_{\text{thr}}$ , we still find an increasing behaviour of  $f_{\text{CNM}}$  with  $\sigma$  but a point of diminishing returns is reached where increasing the turbulence further provides a smaller gain in  $f_{\text{CNM}}$ . This is because the PDF broadens not only to high densities but also to low densities as large voids are being created as counterparts to the dense shocks. Once  $n_0 > n_{\text{thr}}$ , the medium is predicted to be fully in the CNM state at low levels of turbulence. Adding turbulence now typically broadens the density PDF to densities below the CNM threshold, slightly decreasing  $f_{\text{CNM}}$  in favour of the creation of LNM and WNM. This is a theoretical form of CNM destruction by turbulence which was not clearly observed in the simulations.

### 6.6. Comparison to simulation results

To test the accuracy of our model, we want to quantitatively compare with the simulation results. One complication is that galactic disks are not uniform but on average have a Gaussian density profile around a mid-plane density. To partially mitigate this issue, we consider only the inner region of the disk, that is a band between  $z_{\text{midplane}} - 100$  pc and  $z_{\text{midplane}} + 100$  pc.

For each snapshot, we measure the average total density of neutral gas  $n_0$  and the velocity dispersion  $\sigma$  in the mid-plane region to input into our model for  $f_{\text{CNM}}$ . The average density varies over time as the vertical balance in the disk first evolves from the initial conditions to balance the various supporting pressure forces against gravity, and later on adapts to the varying levels of star formation activity. We find values between  $0.35$  and  $1.55 \text{ cm}^{-3}$  across simulations. The velocity dispersion results from the combination of external turbulence driving on large scales and stellar feedback. We find values between  $2$  and  $25 \text{ km s}^{-1}$ . We set  $G_0 = 0.6$ , as this is the value of the constant UV background used in the cooling routines.

#### 6.6.1. Gas phase fractions

In Figure 13, we compare the model predicted phase fraction to the ones measured in the simulations<sup>1</sup>. While our main goal is to model the amount of CNM, we also verify what the model predicts for the LNM. For the low- $\Sigma$  runs, which have fairly low  $f_{\text{CNM}}$ , the prediction is excellent (left panel, bottom left corner). The model accurately describes the trend of increasing  $f_{\text{CNM}}$  with increasing external turbulence driving strength. The agreement is less satisfying for the high- $\Sigma$  simulations. While  $f_{\text{CNM}}$  is predicted correctly in the strong driving case, it is underestimated in the other three simulations. The discrepancy can be slightly reduced by increasing the parameter  $b$  of Eq. 5 for these three runs. This is justified by their higher SFR which lead to more SN feedback, a mostly compressive turbulence driver. Gravitational compression is also stronger when the average density is higher.

The prediction for the LNM fraction is shown in the middle panel. In most cases, it is overestimated and for the high- $\Sigma$  runs we do not reproduce the expected increase with turbulence driving strength. Our model does not take into account the unstable nature of the LNM, which could explain why we overestimate it. Looking at the right panel, we see that the agreement between the model and the simulations is generally good for the sum  $f_{\text{CNM}} + f_{\text{LNM}}$  (or equivalently  $f_{\text{WNM}}$ ). This indicates that once in the LNM state, the gas is likely to quickly cool down further to form CNM.

#### 6.6.2. Density PDF

We can gain more insight in the results by directly comparing the measured density PDF with the modelled one. In Figure 14, we show such a comparison for a selection of example snapshots, one for each simulation. Generally, the WNM peak around  $1 \text{ cm}^{-3}$  is quite well-described by the model. The point of transition to CNM is also captured reasonably well. What does not match well is the shape of the CNM component. In most cases, the model does not reproduce the position of the peak of the distribution. This component of the PDF is also too broad, resulting in an overestimation of the amount of

<sup>1</sup> Note that the measured CNM fractions here are higher than those shown in Figure 6 since here we are limiting ourselves to the densest part of the disk.

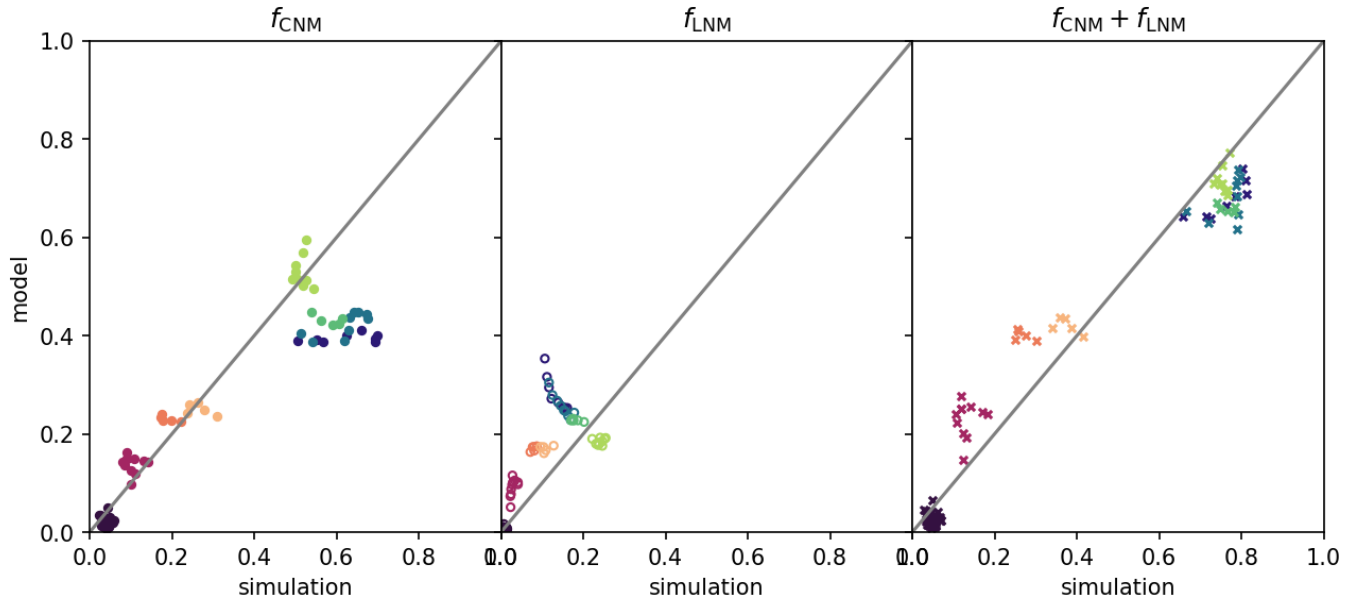


FIG. 13.— Comparison between the mass fractions measured in the simulation with the ones predicted by the model. We show the fraction of CNM (left), LNM (middle) and the sum of both, which is equivalent to  $1 - f_{\text{WNM}}$ .

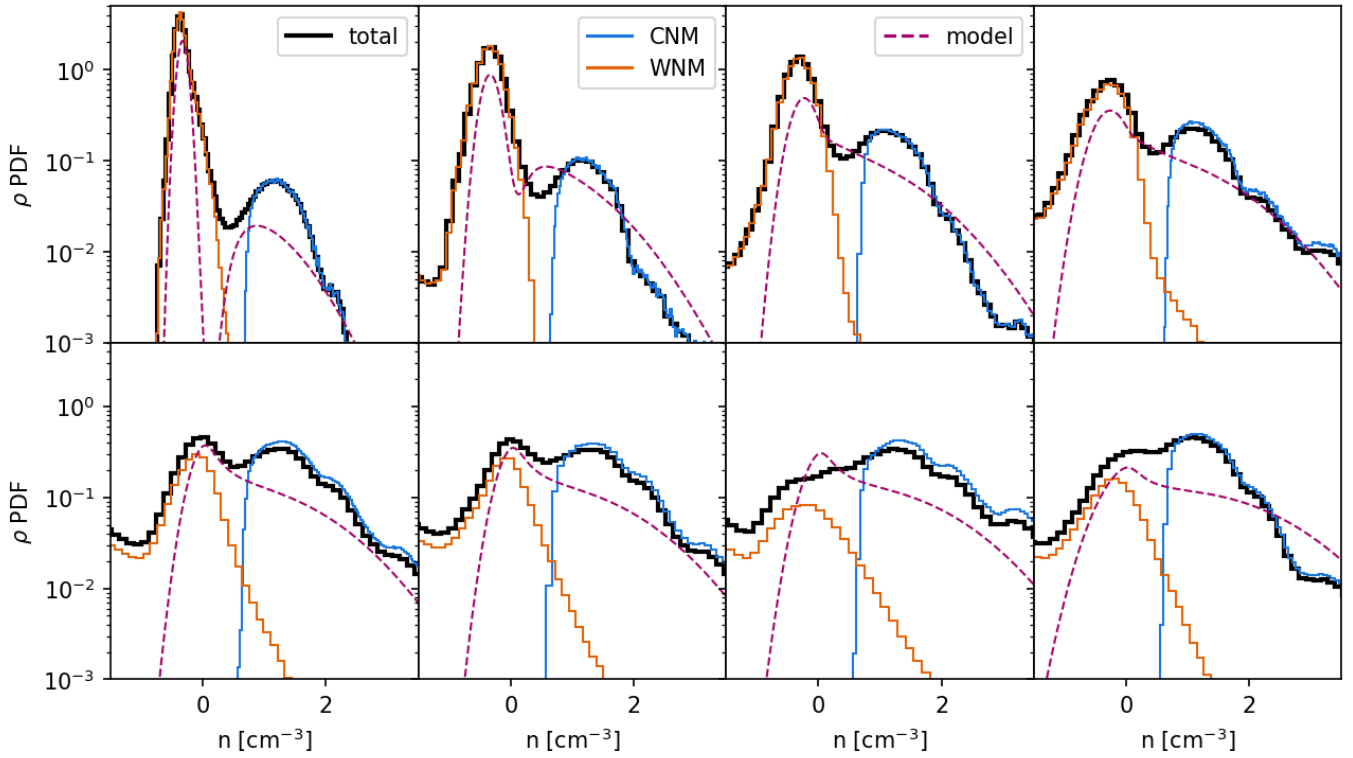


FIG. 14.— Comparison between the measured mass-weighted density PDF and the modelled PDF for a representative snapshot of each simulation. The black curve corresponds to the total neutral gas in the simulation, while the orange and blue curves show the contribution from the WNM and CNM respectively. The dashed line show the model calculated using the average density and velocity dispersion measured in the snapshot. Only the inner part of the disk, between  $-100$  and  $+100$  pc around the mid-plane, is considered for the measurement of the PDF and average properties. The low- $\Sigma$  runs are shown in the top panels, the high- $\Sigma$  ones in the bottom. External driving strength increases from left to right.

dense CNM. Even though the shape of the CNM component leaves much to be desired, the relative importance of CNM versus WNM is well-captured, resulting in a good prediction for  $f_{\text{CNM}}$ .

### 6.7. Caveats and further improvements

Modelling the density PDF of the multi-phase ISM is a difficult problem. Here we proposed a basic model with the aim of self-consistently estimating the CNM fraction. In this, the model succeeds surprisingly well, given that all we did was introduce a density-dependent sound speed. However, more work is needed to accurately describe the full shape of the density PDF. While this is beyond the scope of this paper, we list here some of the ideas we started exploring.

A first avenue is to take into account the magnetic field. [Molina et al. \(2012\)](#) found that this can be achieved by including an additional factor in  $S$ :

$$S = \ln \left( 1 + b^2 \mathcal{M}^2 \frac{\beta}{(1 + \beta)} \right) \quad (8)$$

where  $\beta = P_{\text{thermal}}/P_{\text{magnetic}}$ . When  $\beta < 1$ , this would reduce the width. This dependence is not unlike the dependence on  $b$ , which decreases the width when the turbulence is more solenoidal. We tested several values of  $b$  and found that assuming the turbulence is fully solenoidal ( $b = 0.3$ ) decreases the amount of dense gas while only slightly reducing the CNM prediction. However, this did not solve the problem of the mismatched CNM peak.

It has been pointed out that the PDF may not be exactly log-normal, but has a skewness to it especially at high Mach numbers ([Hopkins 2013](#); [Hennebelle et al. 2024](#); [Brucy et al. 2024](#)). This may be important in the CNM. For the low Mach numbers that characterise the WNM, the log-normal form is a good approximation. We tried replacing the log-normal by this skewed version, dubbed the Castaing-Hopkins PDF ([Castaing 1996](#); [Hopkins 2013](#)). While this produces a better approximation for the transition to LNM and an improved peak shape for the CNM, it introduced a sharp cut-off at high densities and essentially predicted zero gas with densities above  $100 \text{ cm}^{-3}$ . One could argue that at this point gravity would significantly alter the density distribution, producing the additional power-law-like tail ([Burkhart et al. 2017](#)).

The lack of high density gas was not the only issue with the Castaing-Hopkins PDF. While it can reproduce the shape of the WNM component when modelling the high- $\Sigma$  simulations, for the low- $\Sigma$  runs the WNM peak is shifted too far to the right. These experiments indicate that the WNM is better described by a log-normal, while the CNM may consist of a Castaing-Hopkins PDF with an added power-law to include gravity.

That we do not capture the characteristic LNM minimum and CNM maximum, is likely due to the fact that we do not actually take into account that the LNM is an unstable equilibrium. The gas is more likely to be in one of the stable states, that is WNM or CNM. Furthermore, gas that is in the CNM and WNM has a preferred pressure and thus density. This pressure is given by the various vertical balancing forces in a galactic disk, among which feedback from star formation ([Ostriker et al. 2010](#); [Ostriker & Kim 2022](#)). Indeed, in [Figure 5](#) we see the distribution of pressures is broad but peaked. This should somehow be taken into account.

An alternative approach would be to model the WNM and CNM separately and sum the two to obtain the total PDF. Each PDF would be centred around a characteristic density

obtained from a pressure equilibrium model. The width is obtained using the corresponding temperature and optionally a density-dependent velocity dispersion. The problem with this approach is that the CNM and WNM fractions need to be assumed or modelled separately, since  $\text{PDF} = f_{\text{WNM}} \text{PDF}_{\text{WNM}} + f_{\text{CNM}} \text{PDF}_{\text{CNM}}$ . Since our base model gives good results for the CNM fraction, a possibility could be to use this to normalise the individual contributions.

## 7. SUMMARY AND CONCLUSIONS

In this study, we investigate the effect of large-scale turbulence driving on star formation and the thermal balance of the ISM. We analyse a suite of numerical simulations of a  $1 \text{ kpc}^3$  part of a galaxy including stellar feedback in the form of SN and HII regions. The cooling model reproduces a multi-phase ISM with warm and cold neutral phase. The simulation suite explores the star formation behaviour for two initial column density values representative of regions in the Milky Way:  $10.2$  and  $19.1 \text{ M}_{\odot} \text{pc}^{-2}$ . For each subset of simulations, we tested four different strengths of the external large-scale turbulence driving, including a reference simulation without this external component.

We found that the additional turbulence is not only capable of decreasing the SFR, as found in previous studies, but can also enhance it under the right conditions. In the simulations with a lower column density, the SFR increases with increasing external driving strength and the star formation activity is easily an order of magnitude higher than in the case without driving. In the simulations with higher column density, we saw that when the external LS driving becomes significantly stronger than the turbulence injection from SN, the SFR is reduced.

This behaviour is linked to the thermal state of the gas. In the lower column density simulations, increasing the level of turbulence boosts CNM formation which in turn leads to more dense gas for star formation. The CNM fraction increases with driving strength. For the higher column density simulations, the CNM fraction is similar for all runs, while the LNM fraction increases with increasing levels of turbulence as it acts as a perturbing force and promotes phase change. Additionally, the amount of dense CNM is reduced, leading to a smaller star formation rate.

Studying the relation between the SFR and the column density of different mass reservoirs, we further characterise the two regimes. Overall we find a linear relation between the dense gas and the SFR, as in observations. For the lower column density runs we identify an additional correlation between the SFR and the CNM. Our interpretation is that at low densities star formation is limited by the formation of cold gas clouds. At higher densities, an abundance of cold clouds exist and the limiting process is the formation of dense clumps inside those clouds. This change in regime may be an explanation for the observed knee in the Kennicutt-Schmidt relation. This would imply that the scatter in this relation at low column densities is due to variations in the CNM fraction.

To better understand the mechanism behind the generation of CNM by turbulence, we introduce an analytical model containing two main ingredients: the density PDF generated by turbulence and the theoretical temperature-density curve given by the ISM cooling/heating model. To calculate the Mach number, which controls the width of the density PDF, we use a density-dependent sound speed derived from the  $T - \rho$  curve. This leads to a bimodal shape for the PDF, with a narrow WNM peak and a broad CNM component. Their relative

importance then sets the CNM fraction, which we compute by integrating the modified PDF above the density associated with the maximum CNM temperature.

Our analytical model predicts that when the average density of a region is low compared to the threshold density for CNM formation, increasing the level of turbulence will boost the CNM fraction. This is because more shocks and sharper density contrasts are created at higher Mach numbers, resulting in a widening of the density PDF which now extend to values above the CNM threshold. On the other hand, if the average density was already larger than the CNM threshold, all the gas will be in the cold phase at low levels of turbulence. Increasing the turbulent velocity dispersion broadens the PDF both to higher and lower densities, resulting in the generation of WNM and a small decrease in CNM fraction.

Using this model, we are able to predict the CNM fraction from most of the simulations. The match is especially good in the low column density regime where the WNM is the dominant phase. However, when directly comparing the model density PDF to the one measured in the simulations, we see that the shape of the CNM component is not well-described. This shows that more work is needed to accurately model the complex ISM.

#### ACKNOWLEDGEMENTS

This research has received funding from the European Research Council synergy grant ECOGAL (Grant 855130). TC would like to thank all the members of the ECOGAL collaboration for discussions and comments which greatly improved this work. This work also benefited from the Grand Cascade workshop hosted at Institute Pascal in Orsay, France. This work was granted access to HPC resources of CINES and CCRT under the allocation x2020047023 made by GENCI (Grand Equipement National de Calcul Intensif). RSK and SCOG acknowledge funding from the German Research Foundation (DFG) under Germany's Excellence Strategy for the STRUCTURES cluster of excellence in Heidelberg (EXC-2181/1 - 390900948) and also via the collaborative research center (SFB 881, Project-ID 138713538) "The Milky Way System" (subprojects A1, B1, B2, and B8).

#### DATA AVAILABILITY

The simulations will be made available on the Galactica database under the tag LS\_DRIVING.

#### REFERENCES

- Audit E., Hennebelle P., 2005, *A&A*, **433**, 1  
 Bakes E. L. O., Tielens A. G. G. M., 1994, *ApJ*, **427**, 822  
 Bate M. R., Bonnell I. A., Price N. M., 1995, *MNRAS*, **277**, 362  
 Beck R., 2003, *arXiv e-prints*, pp astro-ph/0310287  
 Bialy S., Sternberg A., 2019, *ApJ*, **881**, 160  
 Bigiel F., Leroy A., Walter F., Brinks E., de Blok W. J. G., Madore B., Thornley M. D., 2008, *AJ*, **136**, 2846  
 Bleuler A., Teyssier R., 2014, *MNRAS*, **445**, 4015  
 Bruy N., Hennebelle P., Bournaud F., Colling C., 2020, *ApJ*, **896**, L34  
 Bruy N., Hennebelle P., Colman T., Iteanu S., 2023, *A&A*, **675**, A144  
 Bruy N., Hennebelle P., Colman T., Klessen R. S., Le Yhuelic C., 2024, *A&A*, **690**, A44  
 Brunt C. M., Heyer M. H., Mac Low M. M., 2009, *A&A*, **504**, 883  
 Burkhart B., Stalpes K., Collins D. C., 2017, *ApJ*, **834**, L1  
 Castaing B., 1996, *Journal de Physique II*, **6**, 105  
 Colling C., Hennebelle P., Geen S., Iffrig O., Bournaud F., 2018, *A&A*, **620**, A21  
 Colman T., et al., 2022, *MNRAS*, **514**, 3670  
 Colman T., et al., 2024, *A&A*, **686**, A155  
 Dickey J. M., 1979, *ApJ*, **233**, 558  
 Dickey J. M., Mebold U., Stanimirović S., Staveley-Smith L., 2000, *ApJ*, **536**, 756  
 Draine B. T., 2003, *ARA&A*, **41**, 241  
 Elia D., et al., 2022, *ApJ*, **941**, 162  
 Federrath C., Klessen R. S., 2012, *ApJ*, **761**, 156  
 Federrath C., Klessen R. S., Schmidt W., 2008, *ApJ*, **688**, L79  
 Federrath C., Roman-Duval J., Klessen R. S., Schmidt W., Mac Low M. M., 2010a, *A&A*, **512**, A81  
 Federrath C., Banerjee R., Clark P. C., Klessen R. S., 2010b, *ApJ*, **713**, 269  
 Ferland G. J., 2003, *ARA&A*, **41**, 517  
 Field G. B., Goldsmith D. W., Habing H. J., 1969, *ApJ*, **155**, L149  
 Fromang S., Hennebelle P., Teyssier R., 2006, *A&A*, **457**, 371  
 Gatto A., et al., 2017, *MNRAS*, **466**, 1903  
 Geen S., Hennebelle P., Tremblin P., Rosdahl J., 2016, *MNRAS*, **463**, 3129  
 Glover S. C. O., Clark P. C., 2012, *MNRAS*, **421**, 9  
 Glover S. C. O., Clark P. C., 2014, *MNRAS*, **437**, 9  
 HI4PI Collaboration et al., 2016, *A&A*, **594**, A116  
 Habing H. J., 1969, *Bull. Astron. Inst. Netherlands*, **20**, 177  
 Heiles C., Crutcher R., 2005, in Wielebinski R., Beck R., eds., Vol. 664, *Cosmic Magnetic Fields*. Springer, p. 137, doi:10.1007/3540313966\_7  
 Heiles C., Troland T. H., 2003, *ApJ*, **586**, 1067  
 Heiles C., Troland T. H., 2005, *ApJ*, **624**, 773  
 Hennebelle P., Chabrier G., 2008, *ApJ*, **684**, 395  
 Hennebelle P., Chabrier G., 2011, *ApJ*, **743**, L29  
 Hennebelle P., Falgarone E., 2012, *A&A Rev.*, **20**, 55  
 Hennebelle P., Pérault M., 1999, *A&A*, **351**, 309  
 Hennebelle P., Audit E., Miville-Deschênes M. A., 2007, *A&A*, **465**, 445  
 Hennebelle P., Bruy N., Colman T., 2024, *A&A*, **690**, A43  
 Heyer M. H., Brunt C. M., 2004, *ApJ*, **615**, L45  
 Hopkins P. F., 2013, *MNRAS*, **430**, 1880  
 Iffrig O., Hennebelle P., 2015, *A&A*, **576**, A95  
 Iffrig O., Hennebelle P., 2017, *A&A*, **604**, A70  
 Joung M. K. R., Mac Low M.-M., 2006, *ApJ*, **653**, 1266  
 Kalberla P. M. W., Kerp J., 2009, *ARA&A*, **47**, 27  
 Kennicutt Robert C. J., 1998, *ApJ*, **498**, 541  
 Kennicutt R. C., Evans N. J., 2012, *ARA&A*, **50**, 531  
 Kim C.-G., Ostriker E. C., 2017, *ApJ*, **846**, 133  
 Kim C.-G., et al., 2020, *ApJ*, **900**, 61  
 Klessen R. S., Glover S. C. O., 2016, *Saas-Fee Advanced Course*, **43**, 85  
 Klessen R. S., Hennebelle P., 2010, *A&A*, **520**, A17  
 Krumholz M. R., McKee C. F., 2005, *ApJ*, **630**, 250  
 Krumholz M. R., McKee C. F., Tumlinson J., 2009, *ApJ*, **693**, 216  
 Krumholz M. R., Burkhart B., Forbes J. C., Crocker R. M., 2018, *MNRAS*, **477**, 2716  
 Kuijken K., Gilmore G., 1989, *MNRAS*, **239**, 605  
 Lada C. J., Lombardi M., Alves J. F., 2010, *ApJ*, **724**, 687  
 Leroy A. K., Walter F., Brinks E., Bigiel F., de Blok W. J. G., Madore B., Thornley M. D., 2008, *AJ*, **136**, 2782  
 Longmore S. N., et al., 2013, *MNRAS*, **429**, 987  
 Mac Low M.-M., Klessen R. S., 2004, *Reviews of Modern Physics*, **76**, 125  
 Marchal A., Miville-Deschênes M.-A., 2021, *ApJ*, **908**, 186  
 Martizzi D., Faucher-Giguère C.-A., Quataert E., 2015, *MNRAS*, **450**, 504  
 McClure-Griffiths N. M., Stanimirović S., Rybarczyk D. R., 2023, *ARA&A*, **61**, 19  
 McKee C. F., Ostriker E. C., 2007, *ARA&A*, **45**, 565  
 Miville-Deschênes M.-A., Murray N., Lee E. J., 2017, *ApJ*, **834**, 57  
 Molina F. Z., Glover S. C. O., Federrath C., Klessen R. S., 2012, *MNRAS*, **423**, 2680  
 Murray C. E., Stanimirović S., Goss W. M., Heiles C., Dickey J. M., Babler B., Kim C.-G., 2018, *ApJS*, **238**, 14  
 Ostriker E. C., Kim C.-G., 2022, *ApJ*, **936**, 137  
 Ostriker E. C., McKee C. F., Leroy A. K., 2010, *ApJ*, **721**, 975  
 Padoan P., Nordlund Å., 2011, *ApJ*, **730**, 40  
 Pessa I., et al., 2021, *A&A*, **650**, A134  
 Peters T., et al., 2017, *MNRAS*, **466**, 3293  
 Rathjen T.-E., et al., 2021, *MNRAS*, **504**, 1039  
 Roman-Duval J., Jackson J. M., Heyer M., Rathborne J., Simon R., 2010, *ApJ*, **723**, 492  
 Rosdahl J., Blaizot J., Aubert D., Stranex T., Teyssier R., 2013, *MNRAS*, **436**, 2188  
 Salpeter E. E., 1955, *ApJ*, **121**, 161

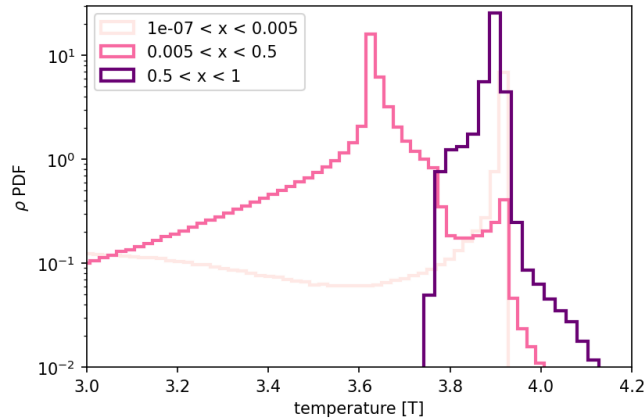


FIG. 15.— Mass weighted temperature PDF for different levels of ionisation fraction  $x$  for an example snapshot.

Saury E., Miville-Deschênes M. A., Hennebelle P., Audit E., Schmidt W., 2014, *A&A*, **567**, A16  
 Schmidt M., 1959, *ApJ*, **129**, 243  
 Schrubba A., et al., 2011, *AJ*, **142**, 37  
 Seifried D., Schmidt W., Niemeyer J. C., 2011, *A&A*, **526**, A14  
 Shetty R., Beaumont C. N., Burton M. G., Kelly B. C., Klessen R. S., 2012, *MNRAS*, **425**, 720  
 Shetty R., Kelly B. C., Rahman N., Bigiel F., Bolatto A. D., Clark P. C., Klessen R. S., Konstantin L. K., 2014, *MNRAS*, **437**, L61  
 Smith R. J., et al., 2023, *MNRAS*, **524**, 873  
 Sun J., et al., 2020, *ApJ*, **901**, L8

Sun J., et al., 2023, *ApJ*, **945**, L19  
 Teyssier R., 2002, *A&A*, **385**, 337  
 Verliat A., Hennebelle P., González M., Lee Y.-N., Geen S., 2022, *A&A*, **663**, A6  
 Walch S., Wünsch R., Burkert A., Glover S., Whitworth A., 2011, *ApJ*, **733**, 47  
 Walch S., et al., 2015, *MNRAS*, **454**, 238  
 Wolfire M. G., Hollenbach D., McKee C. F., Tielens A. G. G. M., Bakes E. L. O., 1995, *ApJ*, **443**, 152  
 Wolfire M. G., McKee C. F., Hollenbach D., Tielens A. G. G. M., 2003, *ApJ*, **587**, 278

## APPENDIX

### WNM TEMPERATURES FOR DIFFERENT IONISATION FRACTIONS

Figure 15 shows a mass weighted histogram of the WNM temperatures in an example snapshot of our simulations. The histogram is split according to the ionisation fraction of the gas  $x$ . We see that gas with an ionisation fraction between 0.5 and 50% has a lower temperature than gas which is more than 50% ionised. This results in two distinct branches of WNM in the phase diagram in Figure 5. This can likely be associated to inconsistent way of calculating the ionisation for the cooling model. fractions. in the treatment of cooling and ionisation, as mentioned in Section 2.5